Alma Mater Studiorum
– Università degli Studi di Bologna –

Dipartimento di Ingegneria Elettrica

Dottorato di Ricerca in Ingegneria Elettrotecnica

– Ciclo XXIV –

Settore Scientifico Disciplinare: ING-IND 31 Elettrotecnica
Settore Concorsuale di afferenza: 09/E1 Elettrotecnica

Numerical analysis of
Dielectric Barrier Discharge

Presentata da:

Dott. Fabio Roveda

Coordinatore Dottorato:

Chiar.mo Prof. Domenico Casadei

Tutor:

Chiar.mo Prof. Carlo Angelo Borghi

Corelatore:

Prof. Andrea Cristofolini

Esame finale anno 2012

CONTENTS

LIST OF FIGURES

LIST OF TABLES

INTRODUCTION

*Se conosci solo il martello ti sembrerá
tutto un chiodo.*

(Giuseppe)

Non equilibrium atmospheric discharges are becoming increasingly studied in recent years. The generation of volumes of plasma dense in radicals and charged species makes this phenomenon highly intersting for engineering applications.

This work focuses on numerical investigations of a widely adopted technique to generate non equilibrium atmospheric plasmas called *dielectric barrier discharge* (DBD).

Impressive progress has been done since W. Siemens first proposed DBD for ozone production in 1857 [2]. Current applications include plasma display panels [3], surface treatments such as film deposition and cleaning [4] and water purification [5], among the others.

This dissertation presents the research carried out at the Department of Electrical Engineering of the University of Bologna and at the Mechanical and Material Engineering Department of the Wright State University of Dayton, OH. The study was focused on numerically simulating the interaction between the ionized gas generated by dielectric barrier discharge and a superimposed gas flow. Results can be useful for several plasma research areas currently followed by the scientific community.

The first and more developed of these is called *electrohydrodynamic interaction* (EHD) [6] [7] [8] [9] and aims to modify the gas flow inside the boundary layer over an aerodynamic profile: such a technique could help enhancing subsonic flow stability without introducing moving parts or extra roughnesses. Another promising field for DBD is *plasma assisted combustion* [10] [11] either in gas turbines or internal combustion engines, to achieve ignition out of the flammable limits and to stabilize the combustion process. Finally, the less known but rather interesting emerging field for DBD are medical skin treatments [12], to heal even serious deseases introducing no thermal effects.

This dissertation mainly addressed to the EHD interaction and includes four chapters. Chapter 1 introduces fundamental physics of plasmas and electric discharges. The following chapter 2 describes DBD in detail and experimental observations. Chapter 3 presents the physical and numerical models adopted to duplicate the discharge phenomenon and computationally simulate charged particles motion. Simulations results are shown in the last chapter for both the plasma kinetic and its interaction with fluidynamics. Also, ch. 4 reports the validation of a diagnostic technique for the EHD interaction introduced by our research group.

CHAPTER 1

PLASMA

*Non c'é badilaccio che non abbia il
suo manicaccio*

(detto popolare)

Abstract Plasma is the most common state of matter in the universe but it is still largely unknown because of its relatively rare presence on earth and its complex behaviour. Nevertheless, many technological applications involve plasma in a variety of fields, ranging from nuclear fusion to surface sterilization. Plasma can be generated through several different techniques according to the properties which are requested: dielectric barrier discharge is a way to produce non equilibrium plasma at atmospheric pressure and its main feature is the coexistence of highly energetic charged particles and low bulk gas temperature, allowing high ionization selectivity and avoiding thermic problems of thermal discharges.
This chapter introduces basic plasma physics, its artificial generation and discusses fundamental DBD characteristics, which is the main subject of the present dissertation.

1.1   Plasmas research in history

W. Siemens introduced dielectric barrier discharge for ozone production in 1857, but first sistematic studies about ionized gases were undertaken a couple of decades later, when J. Crookes developed the tube named after him to study fluorescence phenomena and electrical discharges (fig. 1.1).

Investigations based on the Crookes tube led to major physics discoveries, such as X-rays, identified by W. Röntgen in 1895, and negatively charged particles, discovered by J.J. Thompson in 1897, who also named them *electrons*. New boost to research in ionized gas physics at the beginnign of the XX century was largely due to Irwin Langmuir, who intensively studied high-vacuum tubes and thermoionic emission and first introduced the word *plasma*. He also invented a diagnostic probe (the Langmuir probe) to determine the electron density, the electron temperature and the electric potential of a plasma.

Three main fields arose for plasma research during the XX century.

The chronologically first one was the study of electromagnetic waves propagation in the ionosphere. Radio communications across the Atlantic Ocean were started by Guglielmo Marconi in 1901 and are based on the waves bouncing by the ionosphere. Communications became estremly important at wartime for armies and navies, so big efforts were made to study the partially ionized layer of atmposphere which reflects EM waves.

The second stage of plasma research was related to astrophisics. It was understood that much of the intergalactic and interstellar medium consists of plasma and getting to know them well required a better knolwledge of plasma physics. This is particularly true for the Sun, whose intensely magnetic sunspots produce many intricate plasma phenomena which affect the Earth environment also.

The third field of study for plasma is related to nuclear fusion for power

Figure 1.1: Crookes tube and power generation system.
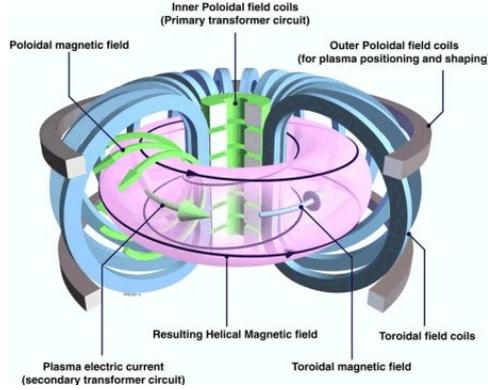
Figure 1.2: Magnetic plasma confinement developed for ITER.

generation. Highly energetic atoms need to coexist in an extremely dense environment to achieve positive energy balance from fusion. Such a great energy density would destroy any material casing meant to contain it, but it also ionizes the gas, making it plasma if properly managed. This plasma can be magnetically confined for creating suitable fusion conditions involving no material shielding.

Research on fusion plasma is one of the most challenging endeavors undertaken from the scientific community in the last century and led to several experiments, but there is still a long way to go for commercial fusion energy. The ultimate research machine is called ITER and is scheduled to be operated first in 2019, aiming to be the first fusion reactor to generate a positive net energy balance: its magnetic configuration is shown in fig. 1.2.

1.2   Plasma

Plasma is a *quasineutral* conductive ionized gas, exhibiting a *collective behavior* and a *plasma frequency* greater than the electron-neutral collision frequency.

It is useful to introduce the *Debye lenght* λ_D and the *plasma frequency* ω_p to quantify the above criterias:

$$\lambda_D = \left(\frac{\epsilon_0 kT}{ne^2}\right)^{1/2} = 69.0 \cdot \left(\frac{T}{n}\right)^{1/2} \quad m \tag{1.1}$$

$$\omega_p = \left(\frac{ne^2}{\epsilon_0 m_e}\right)^{1/2} = 2\pi \cdot 8.97 \cdot n^{1/2} \quad s^{-1} \tag{1.2}$$

where T is the plasma temperature (in K), n is the electron number density, m_e is the electrons mass.

....

The Debye lenght determines the sphere of influence of a test charge immersed in the plasma. It tells about the screening effect that the plasma has on the electric field: the Coulomb potential due to the test charge drops for distances greater than λ_d from it and no significant charge separation occurs outside the Debye sphere.

The collective behavior arises if many charged particles are inside the Debye sphere, so that perturbations affect a large number of particles: there is no need to consider two body collisions but a mean electromagnetic field correctly describes interactions between charged particles. The number of particles inside the Debye sphere is called the *Debye number*, N_D, and $N_D \gg 1$ must hold for the collective behavior.

Quasineutrality involves the overall electric charge of plasma. Even though free electrons and ions are present, the system is globally neutral over a length scale much larger than the Coulomb interaction lenght scale λ_D, because of shielding effects.

The electric charge density fluctuates harmonically around the equilibrium condition according to the plasma composition, and the fluctuation frequency is the plasma frequency ω_p, describing how fast the plasma reacts to distortions from electric neutrality . If perturbations are faster than the plasma frequency, free electrons cannot contrast it and deviations from quasineutrality are not balanced. The last condition for defining plasma ensures electrical phenomena be dominant over ordinary gas kinetic: the plasma frequency must be grater than electron-neutral collision frequency.

Typical values of λ_D and ω_p are shown in table 1.1 for a variety of plasmas, as well as other meaningful plasma parameters.

Table 1.1: Representative densities, temperatures and derived plasma parameters in a variety of environments [1]

Plasma	n_e (m^{-3})	T (K)	λ_D (m)	N_D	ω_D (s^{-1})
Gas discharge	10^{16}	10^4	10^{-4}	10^4	10^{10}
Tokamak	10^{20}	10^8	10^{-4}	10^8	10^{12}
Ionosphere	10^{12}	10^3	10^{-3}	10^5	10^8
Magnetosphere	10^7	10^7	10^2	10^{10}	10^5
Solar core	10^{32}	10^7	10^{-11}	1	10^{18}
Solar wind	10^6	10^5	10	10^{11}	10^5
Interstellar medium	10^5	10^4	10	10^{10}	10^4
Intergalactic medium	1	10^6	10^5	10^{15}	10^2

The definition of plasma includes an extremely wide range of ionized gases. Some natural and man-made plasmas are categorized in fig. 1.3 by electron number density and bulk gas temperature.
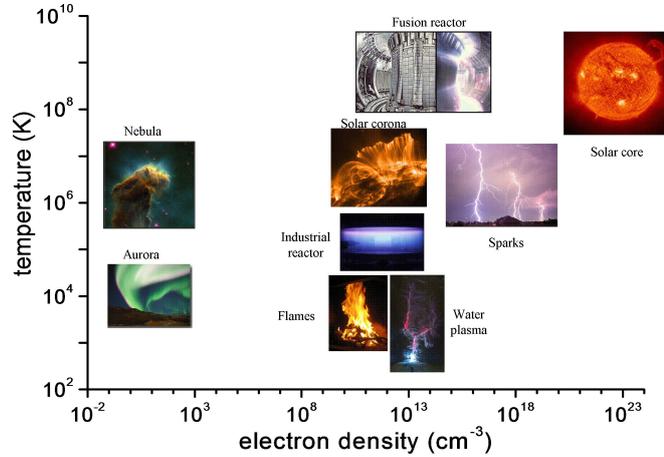
Figure 1.3: Plasmas varying in bulk gas temperature and electron number density.

The major distinction is traditionally made between *thermal* plasmas and *non-thermal* ones. Thermal plasmas can be found for example in nuclear fusion, electric arcs for metal cutting and waste disposal: their distinguishing feature is the thermal equilibrium between ionized particles and the the bulk gas, providing an high degree of ionization because of the large energy involved. However, efficiency and applicability of these discharges are affected by low ionization selectivity, quenching and cathode wearing out problems. On the other hand, non-thermal (*cold*) plasmas like low pressure glow or corona discharge consist of charged particles whose energy is much less than neutral ones and the gas temperature is consequently low. High excitation selectivity and limited thermic issues give cold discharges interesting advantages over thermal palsmas. Nonequilibrium plasmas are currently generated for water purification, antimicrobial treatment of food, displays panels, fluorescent lamps and semiconductor device fabrication, including surface cleaning, etching and vapor deposition.

1.3   Generation of artificial plasma.

Plasma is generated by supplying energy to a neutral gas to ionize molecules and create electron-ion pairs. There are several ways of providing energy to the gas [13]:

- by applying an electric field to start the avalanche mechanism;

- by moderating energetic beams in a neutral gas reservoir to energize it. Different kinds of particles can be adopted:

    - neutral beams, which are not affected by electromagnetic fields;

    - charged particles, especially electrons;

    - photons;

- by supplying thermal energy (for example in flames) using exothermic chemical reactions as primary energy source;

- by adiabatically compressing the gas to heat it up to the point of plasma generation.

The most common techniques currently adopted for plasma generation can all be ascribed to the first of the above.

Electric discharges start from free charges naturally present in neutral gases, due to cosmic radiation and natural radioactivity. These particles are accelerated by the externally applied electric field and gain kinetic energy which is lost in ionizing collisions with neutrals. If the ionization rate is large enough to balance recombination processes, the avalanche process starts and the *discharge* is generated (see the following paragraph for more detail).

Discharges are classified as *dc discharges*, *ac discharges* and *pulsed discharges*; a particular class, different from the previous ones, is *dielectric barrier discharge (DBD)*. All kinds of discharge will be briefly described in paragraphs 1.4 and 1.5 after a short introduction to the avalanche process, the basic phenomenon common to all of them.

Electric breakdown and electron avalanches

The avalanche process is the mechanism for primary electrons moltiplication and the basic phenomenon for every electric discharge.

Consider a uniform electric field E applied to a plane gap of length l between two electrodes. The avalanche starts from primary electrons casually generated in this gas gap by natural radiation or photoelectric ionization. We consider one electron generated near the cathode surface, which is accelerated by the electric field E and transfers its kinetic energy to other molecules by collisions.

Part of the transferred energy causes ionization, i.e. the creation of an electron-ion pair. Electrons released from the ionization are also accelerated and collide neutrals generating in turn new free electrons, and so on. This chain of ionizations is called *avalanche*.

The ionization rate coefficient $k_i = k_i\left(\frac{E}{n_0}\right)$ is the number of ionizations caused by each primary electron per second per unit number density of neutral particles. It is useful to refer to the *first Townsend ionization coefficient* $\alpha = \frac{d\,n_e}{d\,x}$

. . . .

to quantify the avalanche process.

α_i is related to k_i as follows:

$$\alpha = \frac{\nu_i}{v_d} = \frac{k_i\,n_0}{v_d} = \frac{k_i\,n_0}{E\,\mu_e} \tag{1.3}$$

where ν_i is the ionization frequency per electron, v_d is the electron drift velocity and μ_e the electron mobility. According to this definition, the amount of electrons produced by one primary electron generated near the cathode during its drift to the anode is $e^{\alpha l}$, while the number of positive ions is $e^{\alpha l}-1$. Reattachment and recombination phenomena are considerable in electronegative gases especially and are described by the *second Townsend coefficient* β:

$$\beta = \frac{\nu_a}{v_d} = \frac{k_a\,n_0}{v_d} = \frac{k_a\,n_0}{E\,\mu_e} \tag{1.4}$$

where ν_a is the reattachment frequency per electron and k_a is the reattachment rate coefficient. Both α and β are exponential funcitons of the reduced electric field $\frac{E}{n_0}$. Ionization usually exceeds recombination and reattachment for high values of the reduced electric field, so it is usually the only one considered in short gaps [14].

Accounting for ionization, reattachment and recombination, the number of ions produced in the whole gas gap per primary electron generated near the cathode is $e^{(\alpha-\beta)l} - 1$.

Positive ions generated in the gap drift under the effect of the electric field and eventually strike the cathode surface causing *secondary electron emission*. This phenomenon is described by the *secondary emission coefficient* γ. Each primary electron produces $\gamma\big(e^{(\alpha-\beta)l} - 1\big)$ secondary electrons at the cathode, which in turn start a new avalanche: the discharge is self-sustained if the amount of secondary electrons generated from one primary electron is equal or greater than 1. The *electric breakdown* is the establishment of a self-sustained discharge, which means that every electron lost in the system (for any reason) is replaced by at least a new one, generated from the discharge itself by means of secondary electron emission.

According to the above definitions, the breakdown condition is then:

$$\gamma\big(e^{(\alpha-\beta)l} - 1\big) = 1 \tag{1.5}$$

Critical electric field: the Paschen curve

The breakdown condition (1.5) accounts for electric and topological parameters of the system. It is possible to rearrange eq. (1.5) to emphasize the critical electric potential for breakdown V_b as a function of the parameter pl, where p is the pressure. In a simplified system where β is neglected,

$$V_b = \frac{B\,pl}{C + \ln pl} \tag{1.6}$$
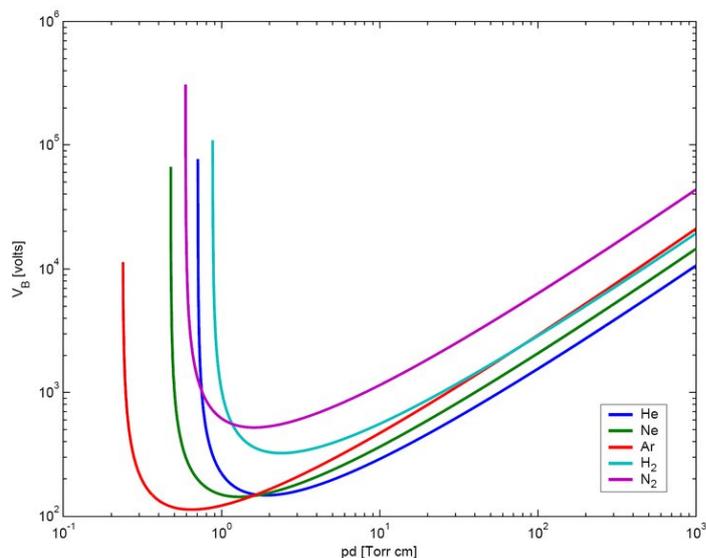
Figure 1.4: Paschen curves for different gases. The distance between electrodes is indicated here as d instead of l.

where the constants B and C depend on the gas composition and the chatode material. The relationship between the breakdown voltage and the parameter pl is usually referred to as the *Paschen law*: some examples for different gases are shown in fig. 1.4.

  The Paschen curve has a minimum voltage point, corresponding to the easiest breakdown condition:

$$V_{min} = \frac{eB}{A} \ln 1 + \frac{1}{\gamma} \tag{1.7}$$

$$pl_{min} = \frac{e}{A} \ln 1 + \frac{1}{\gamma} \tag{1.8}$$

where $A = \frac{e^C}{\ln \frac{1}{\gamma}+1}$ is a constant for a given gas. The minimum voltage point is reached if the optimum balance between the opposite effects of pressure and gap length l is achieved. If the pressure is too low, collisions are unlikely and ionization doesn't take places, so the avalanche is harder to achieve (higher V_b is necessary). On the other hand, electrons collide too frequently with neutral particles and cannot gain enough kinetic energy to ionize them if p is too high. With respect to the distance between the electrodes l, if it is too short the avalanche cannot develop because too few collision can happen during electron drift motion from cathode to anode; if the distance is increased too much, recombination is enhanced and higher voltage are required to increase to mitigate its effect.

. . . .

1.4   Discharges

Three primary electrical plasma sources are distinguished:

1. DC discharges

2. Inductively coupled discharges

3. Dielectric Barrier Discharge

1.4.1   DC discharges

DC discharge regimes vary depending on power supply conditions. An effective description of this behavior is given by picture 1.5.
Low current (10^{-18} to $10^{-5} A$) non self-sustained regimes are said *Townsend discharges* and include the widely industrially applied *corona discharges*; the applied voltage is higher than other DC regimes because conductive channels are not formed and the conductivity is low. Applications for Townsend discharges are usually found in gas phototubes, ozone production, removals of chemical species from surfaces, sanitization of pool water and drag reduction among the others.
The breakdown voltage for transition to self sustainability is reached by increasing the current density, so the discahrge changes to a *glow* regime, characterized by a lower voltage than the corona discharge because the conductivity is significantly increased. The name of this kind of discharge is due to light emission, which is exploited in neon lamps and plasma display panels.
An *abnormal glow* discharge develops as the current density is increased further until the voltage drops and eventually the discharge turns into an *electric arc*, characterized by low voltage, high current densisties and high power absorption compared to both Townsend and glow discahrges. The arc regime is the only one which can be achieved at ambient pressure, while lower power discharges are usually obtained in closed discharge vessels under vacuum conditions. Electron number density for electric arcs can be as high as $10^{24} m^{-3}$.
Applications for thermal arcs include metal welding and cutting, waste disposal and furnaces, among the others.

 Pulsed DC discharges can be considered a particular kind of DC discharges and have some advantages over regular DC regimes portrayed in fig. 1.5. Basically, they can be operated at higher power and can be controlled more effectively because one more working parameter is available, the duty cycle. Pulsed discharge are used in gas pollution control, PET bottles sterilization and plasma focus apparatus for nuclear fusion research.

....
—————————————————————
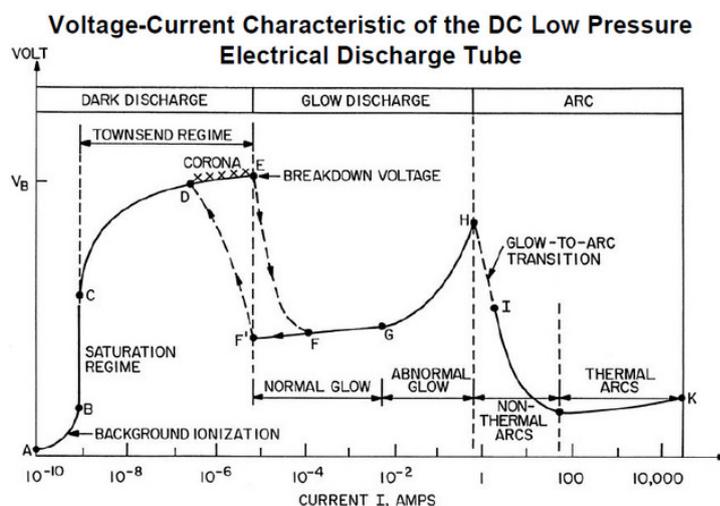
Figure 1.5: V-I regimes for DC discharges.

1.4.2 Inductively coupled discharges

Inductively coupled plasmas (ICP) technology has been studied for longer than a hundred years since it was developed first by J.W. Hittorf in 1884. ICPs are obtained by applying a time varying magnetic field to the working gas, so that ionizing inductive electric field is generated in the discharge area. Typical ICP devices consist of a reactor chamber usually made of quartz, open at the ends for gas injection and extraction. The quartz container is surrounded by a magnetic coil supplied with AC current, so that the induced electric field accelerates free electrons in the discharge region along the coil axis and sustains the plasma. The whole system can be operated either at ambient or lower pressure; Argon is usually adopted as working gas to limit recombination effects. AC power frequencies vary from some kHz to tens of MHz and electron densities as high as $10^{18}m^{-3}$ can be achieved. The inductive circuit element can either be a spiral-like or a helical conductor. Fig. 1.6 shows helical ICP arrangments for coupler (left) and resonator (right), both provided with Faraday-shielded reactor chambers to aviod capacitive coupling and tuning systems to adjust operative regime to resonance.
The main advantage of ICPs over DC plasmas is that no contamination from electrodes wearing out occurs and the plasma is more pure.
Applications for ICP include microelectronics, chemical spectroscopic analysis and thermalization of gases to produce thrust from a plasma jet.
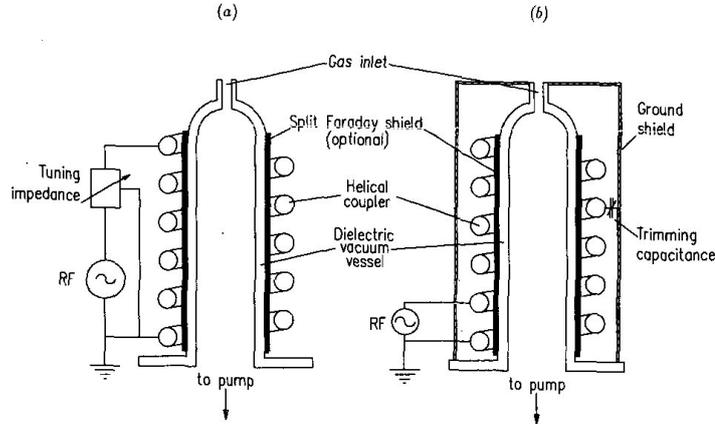
Figure 1.6: Cross sectional schematic diagrams of two inductively coupled plasma reactors: (a) helical coupler and (b) helical resonator [15].

1.5 DBD

Dielectric Barrier Discharge (DBD) is achieved by supplying proper AC voltage to an electrode pair and covering at least one of them with an insulating material. DBD most outstanding feature is the capability of avoiding spark formation and transition to arc in streamers channels, because charged species accumulation on the dielectric layer limits the electric field in the gas gap and microdischarges lifespan cannot exceed few hundreds of nanoseconds.

The presence of the dielectric layer precludes DC regimes and DBD is usually operated at frequencies between 1 and 500 kHz and voltage of some kV. Three characteristics of DBD are of particular interest for engineering applications. First of all, AC regimes coupled with the self-limiting behavior of DBD provide strongly non-equilibrium conditions, generating electrons more energetic than the bulk gas: these electrons can be exploited for selective ionization and several other processes. Second, DBD operates at atmospheric pressure and at considerable power level, so no vessels or containers are usually requested for treating even large volumes of gas. Finally, the power supply system doesn't have to be sophisticated, being AC voltage quite easy to be generated. Applications for this technology range from the well known ozone production introduced by W. Siemens to CO_2 lasers, excimer radia-

tions generation, thin film deposition processes and plasma displays.

In recent years, significant research efforts have been directed to three areas for DBD technology which are suitable applications for the numerical work presented in this dissertation:

- EHD for separation control over airfoils;

- medical skin treatments;

- plasma assisted ignition and combustion.

1.5.1 Electrohydrodynamic interaction

Asymmetric DBD configuration made by so-called *plasma actuators* (fig. 1.7) can either induce flow motion in an initially quiescent room air or modify boundary layer flow properties of a superimposed gas flow. This phenomenon is called *Electrohydrodynamic* interaction (EHD) [6, 16, 17]. EHD is a promising tool to control the boundary layer properties of a subsonic flow and is especially studied for separation delay (stall control) or laminar to turbulent transition enhancer. For the last application, it would be an useful alternative to extra roughnesses placed on airfoils, involving no moving parts, short response time and lower power consumption. Major issues affecting EHD effectiveness are anyway related to electrodes and dielectric currently unaccettable wearing rate.

The alternative electric field obtained by means of the electrode configuration shown in fig. 1.7 has both a component parallel to the dielectric surface and one perpendicular to it, so gas ionization in streamers channels and charged particles surface acceleration take place simultaneously. Coupling between the Coulomb force and the gas body force is due to charged species collisions with neutral particles, providing momentum exchange. The complex interaction of charged species in a non-thermal plasma with the bulk gas and the dielectric barrier is the underlying physical aspect which has to be understood in order to improve plasma actuators efficiency and to make them reliable enough for aeronautical applications.

1.5.2 DBD skin treatments

Several DBD techniques have been studied over the last few years for medical and biological applications of non thermal plasmas [12]. Two different approaches are distinguished. In *direct* treatments (fig. 1.8), one electrode is the surface to be treated, i.e. the skin. In *indirect* treatments, a gas flow blows discharge products to the skin and the discharge is generated between two distinct electrodes. Non-thermal plasmas produce highly energetic particles in a globally cold gas, so that no heating effects are involved while reactive properties of radical species are retained. Applications in this field
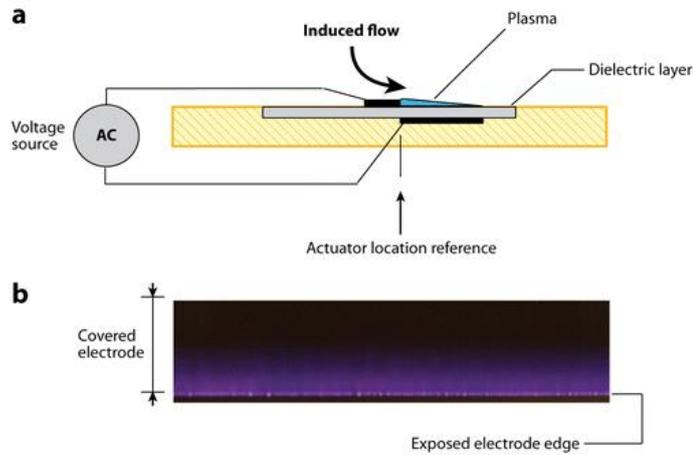
Figure 1.7: EHD actuator (top) and discharge regime (bottom).

are, for example, selective inactivation of unhealthy cells, blood coagulation, killing of parasites, bacteria, fungi, and viruses on living tissues.
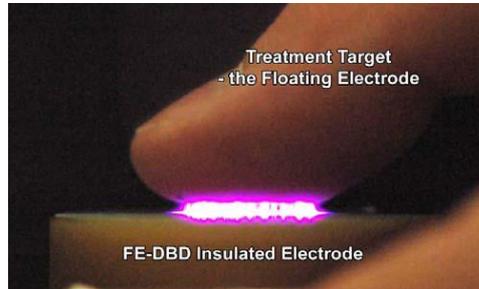
Figure 1.8: Medical applications of non thermal plasmas: direct treatment.

1.5.3   Plasma assisted ignition and combustion

Low temperature plasma of nonequilibrium gas discharges are nowadays widely studied for ignition and combustion enhancement in both internal combustion engines and gas turbines; some studies are also performed to improve waste plasma treatments [10]. DBD affects the discharge enviroment by introducing reactive species (free radicals), heating the gas, providing momentum to the gas and generating shocks and instabilities. All these factors can be exploited to make ignition possible out of the flammable limits and

to stabilize the flame in buondary conditions. This research field is highly promising to increase engines efficiency, reducing pollutant production and limiting operating costs. On the other side, making combustion possible out of the falmmable limits widens the operative range of aircraft turbines and allows to fly at higher altitudes. DBD is one of the plasma sources adopted to generate nonequilibrium plasmas suitable for this application and one example is shown in fig. 1.9.
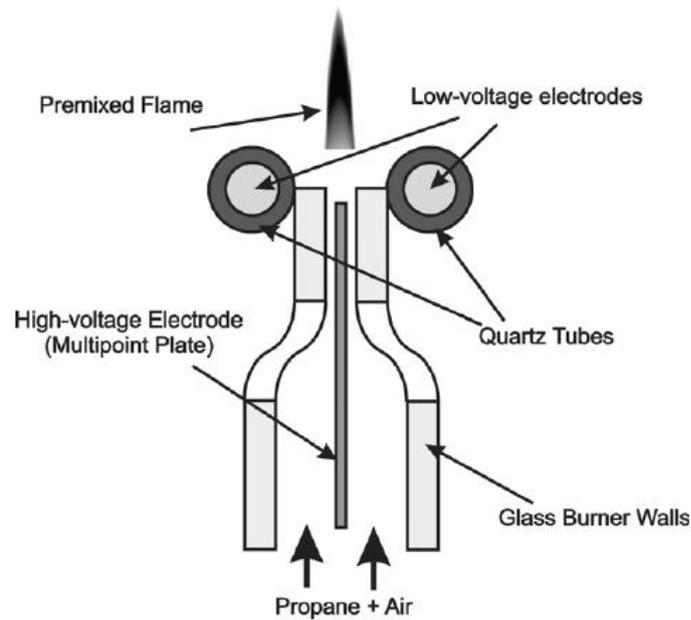
Figure 1.9: DBD apparatus for plasma assisted ignition.

CHAPTER 2

PHENOMENOLOGY OF DBD

*Il popolo deve combattere per la sua
legge come per le mura della cittá.*

(Eraclito)

Abstract This chapter describes DBD features by introducing experimental investigations made during the last 15 years, expecially in the aerodynamics field. Different aspects have been considered and many techniques have been adopted to understand the rather complicated physics behind non-equilibrium discharges.

2.1   Introduction

DBD is an effective technique to generate steady-state, high pressure, volumes of plasma. Supplying AC power to the electrodes results in random microdischarge generation and streamers propagation in the gas gap. The presence of the dielectric barrier determines electric charge accumulation on the dielectric itself and progressively reduces the electric field during every half AC cycle, so that the streamers filaments are eventually quenched after a lifetime of some hundreds of nanoseconds [18].

Plasma EHD actuators are particular DBD devices implying nonequilibrium electric discharge between two asymmetric electrodes of which one is exposed to the air (or gas flow) and the other one is covered with an insulating layer (fig. 2.1). They have been intensively studied for aerodynamic application over airfoils, to modify and control boundary layer flow properties. These studies are a major source for physical and numerical knowledge of DBD and the following discussion is mainly based on them.

Many different settings for EHD actuators have been studied. The typical configuration is shown in fig. 2.1. The dielectric layer is made of teflon, kapton, glass, Teflon or PVC and usual thickness is some mm. Electrodes are generally made of copper or alluminium and the buried one is grounded. Their height (y-direction) is usually not greater than some hundreds of μm; the grounded electrode length x-wise is important for the plasma size and can be up to some cm, while the x-size of the upper one doesn't affect the discharge properties. The x-gap between electrodes ranges from 0 to some mm. Some experiments report about 3-electrodes plasma actuators where an additional uncovered electrode is placed downsteram with respect to the flow. It is usually biased to generate further thrust in the x-direction.

The power supply is generally sinusiodal AC current, with frequencies on the order of kHz and voltages as high as some kV. Many different waveforms have been tested, like triangle waves, square waves, sawtooth waves and rectangular pulses, even positively or negatively biased. It is important to note that periodically reverse the applied voltage leads to great improvement in the actuator efficiency, probably because of uncharging the dielectric surface.

2.2   Experimental evidences of EHD

Optical analysis of DBD

Several works demonstrate the microdischarge nature of DBD [19], [9], [18] through time-resolved imaging. Typical values of microdischarges lifespan is around tenth of microseconds because the insulating layer prevents the streamer to arc transition.

Investigations by Enloe et al [20], [21]. were meant to understand how the applied voltage and AC frequency affect the plasma light emission. Light
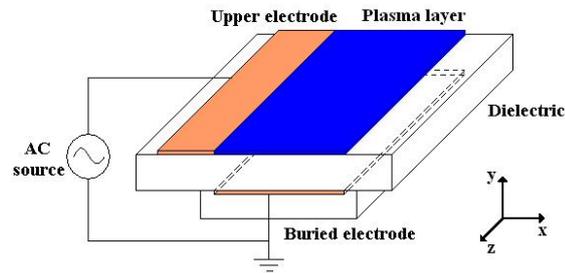
Figure 2.1: Plasma actuator for EHD and frame of reference.

emission is taken as effective indicator of plasma density since recombination, which is responsible for it, is approximately 10^5 times more frequent than AC inversion and it can be assumed to happen in a *frozen* electrical condition. The ionized air is always observed only over the embedded electrode and appears quite uniform in color and distribution (fig. 1.7) to the unaided eye. However, utilizing a photo-multipier tube (PMT) arrangment to document the space-time evolution of light emission, a more complex behavior arises. The PMT was positioned over the dielectric surface like shown in fig. 2.2.
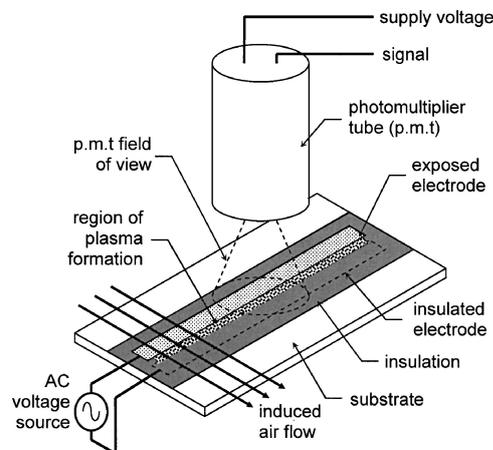
Figure 2.2: PMT setup for light emission measurements.

The study conducted in the works by Enloe demonstrates that plasma is formed only in part of the AC cycle, consistently with the assumption that the Townsed discharge occurs only if the applied voltage is larger than a given threshold.

Uneven distribution of plasma density (PMT signal) between the positive and the negative half cycles is shown in fig. 2.3. When the applied voltage is positive (i.e. the upper electrode has a higher voltage than the embedded

one), electrons are attracted by the bare electrode and pushed away from the dielectric: secondary emission takes place on the dielectric layer. On the contrary, secondary emission occurs on the conductive material during the negative phase, since electrons are repelled from it. The asymmetric behavior is certainly responsible for any difference in physical properties between the positive and the negative half cycles. A possible and more detailed explanaton for irregularity is that the bare electrode acts as an infinite source of electrons during the negative phase and provides them more regularly than the dielectric layer does in the positive phase.

Irregularities are also detectable by comparing high-speed camera images for the positive and negative AC semi-periods (fig. 2.4) and are in excellent agreement with PMT results, showing more diffuse and uniform ionization during the negative half cycle (top) rather than the positive (bottom).
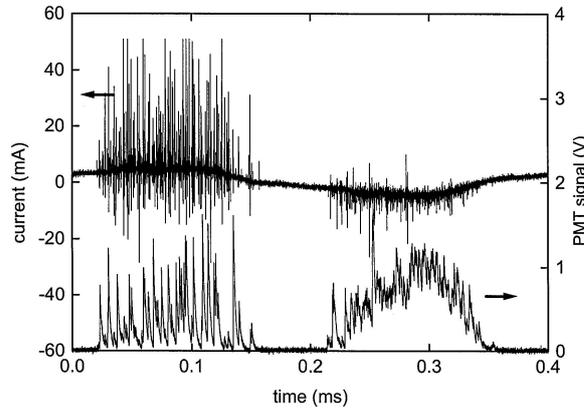
Figure 2.3: Current (top line) and light emission intensity (bottom line) during an AC cycle. The positive driven phase ranges form 0.0 to 0.2 ms and the negative one form 0.2 to 0.4 ms.

Schlieren imaging - vortex visualization

Schlieren visualization is an effective, non invasive tool to show mass density gradients in cold plasmas. The vortex generated during the starting transient can be studied and its propagation investigated. Cristofolini et al. [22] determined the eddies velocity at 4 different power supply regimes, the AC frequency being equal and found it to be about $1.5\,m/s$ if the dissipated power is $140\,W/m$. The starting transient of EHD interaction visualized by means of Schlieren diagnostics is shown in fig. 2.5 at four time levels.
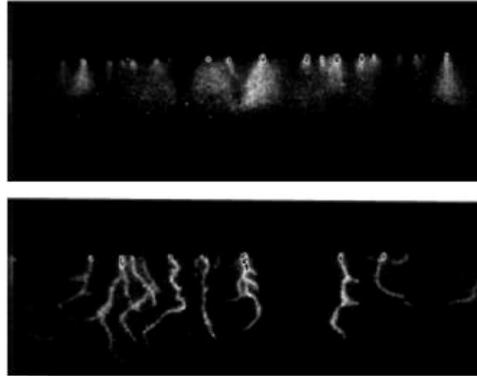
Figure 2.4: Difference between the negative (top) and positve (bottom) phase of DBD.
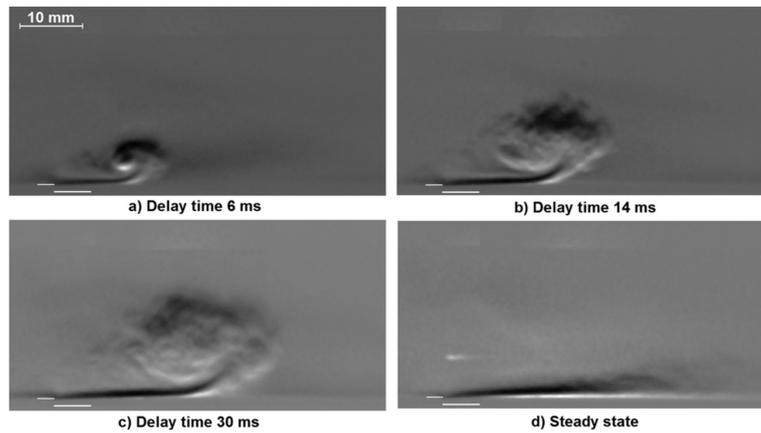
Figure 2.5: EHD starting transient, vortex visualization.

Electrical behavior of DBD

AC sinusiodal waveform is the most common power supply regime adopted for DBD, because it can be generated with ease. Nevertheless, several different voltage regimes have been studied. It is to be noted that implementing the optimum waveform implies a deep understanding of the discharge physics. More precisely, there is an open question about the effect of voltage polarity on the body force. Some researchers believe that DBD operates in so-called PUSH-PULL mode, meaning that the force exerted on the bulk gas reverses according to the voltage polarity. Some others are instead for a PUSH-push mode, where the force doesn't change direction but just reduces its magnitude during the negative phase. Finally, more recent studies suggest a push-PUSH mode where the strongest thrust is produced during the

negative phase.

Current and voltage versus time plots for the actuator configuration of fig. 2.1 on page 22, operated with sinusoidal power supply, are shown in fig 2.6. Peak to peak voltage is 40 kV and AC frequency is 1 kHz. The current plot reports the total current in the gas gap; its conductive component is associated with streamers formation while the displacement component is due to dielectric charging and related capacitive effect. Current intensity can be up to $15\,mA/m$. Streamers are stronger and more irregular during the positive half cycle, consistently with what reported in the previous paragraph.
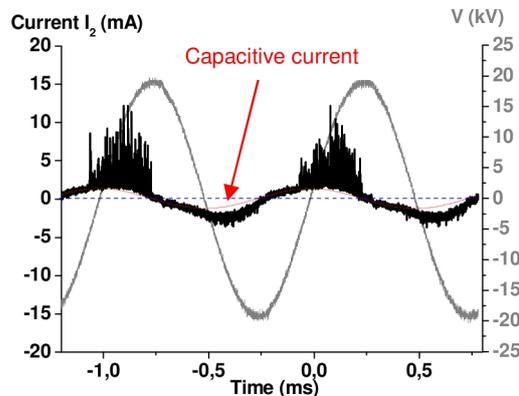

Figure 2.6: Voltage and current regimes for sinusoidal AC power supply.

Sawtooth waveform (fig. 2.7a) with positive and negative mean value were investigated by Enloe [20] to demonstrate that thermal effects cannot be responsible for the thrust induced by DBD. In fact, supplying a certain amount of power leads to different thrust effects according to the polarity of the sawtooth waveform, proving that the dissipated power is not the only phenomenon responsible for induced flow motion.

Pulsed power supply (fig. 2.7b) with either positive or negative bias was studied by Opaits et al. [23] to develop optimized operating techniques for DBD. The idea behind this approach is that momentum trasfer is mediated by ions, which are produced by voltage peaks. Once they are produced, ions are accelerated by the electric field and then transfer momentum by collision with neutrals. Experiments by Opaits are meant to produce a large amount of ions with high frequency pulses and then accelerate them between pulses with a constant, superimposed bias. However, it was understood that after some hundred pulses the surface charge builds up and improvements towards AC sinusoidal power supply becomes negligible. The solution proposed was to alternately reverse the bias polarity and significant improvement was achieved. This waveform also introduces more flexibility in the DBD opera-

(a) Sawtooth voltage
waveform studied in [20]

(b) Pulsed voltage waveform
studied in [23]
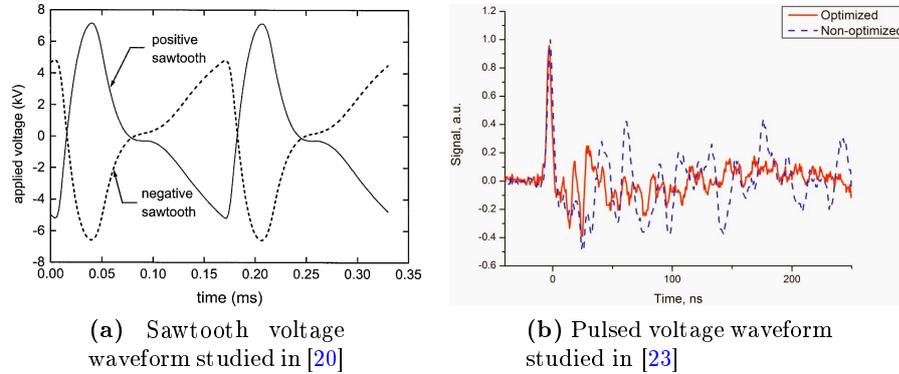
Figure 2.7: Examples of AC regimes studied for DBD applications.

tion.

The effect of AC frequency has been widely studied and works were proposed reporting frequencies ranging from some tenth of *kHz* up to several *MHz*. Many believe that the best solution for fluid dynamic purposes is to apply AC frequency similar to characteristic times of the flow speed, bounded to the speed of sound. Opaits [23] and Enloe [21] propose then optimum AC frequency of some *kHz*.

Flow velocity measurements

The capability of plasma actuators to induce motion in a quiescent gas and to accelerate flows has been widely proved.

Borghi et al. [7] showed that sinusoidal AC power supply of $5.4\,kV$ can accelerate still gas up to around $4\,m/s$. The wide investigation involved comparisons with different supply frequencies, ranging from 3 to $9\,kHz$ for still air and $1, 15, 31\,m/s$ free flow velocity. Results of this study are portrayed in fig. 2.8 and reasonably show that the considerable effect of EHD interaction becomes negligible for high flow speed.

Moreau et al. [8] studied the relation between induced flow speed and current density, as shown in fig. 2.9 for $5\,m/s$ free flow speed. Momentum transfer is increased considerably by increasing the time averaged current density.

Force measurements and effect of dielectric material

A diffuse study aimed to understand the role played by the insulating material in DBD was carried out by Flint et al. [24]. Fig. 2.10 reports the thrust-voltage relation for different dielectric materials and thickness, so that the thrust is assumed as metric for comparisons. All data sets are truncated

. . . .
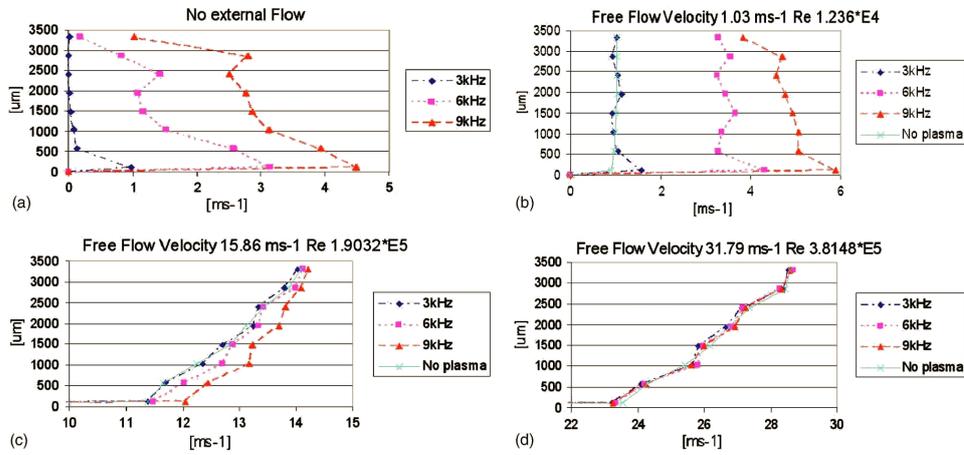
Figure 2.8: Induced flow motion for different values of AC frequency and free flow velocity.
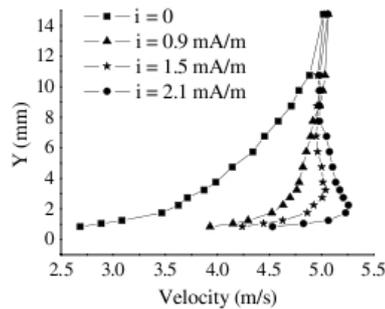
Figure 2.9: Flow velocity in the boundary layer as a function of the height above the dielectric for different values of discharge current

when saturation conditions are achieved, which means that no increase in the measured force is obtained by increasing further the applied voltage. The first feature highlightened by the picture is straightforward: all conditions being equal, smaller thickness leads to higher electric field and hence to higher thrust (see for example $3.18\,mm$ Telfon vs $6.35\,mm$ Teflon). Another characteristic pointed out by the plot is related to the dielectric permittivity and implies that higher the dielectric constant, higher the thrust, other things being equal. The third and probably less predictable information is about the maximum thrust achievable, which corresponds to saturation condition and is shown to be higher for thicker dielectric barriers made with materials having low dielectric constant. This last effect is probably due to

different charge accumulation characteristic for each dielectric.

The work also provides information about the overall force produced by DBD.
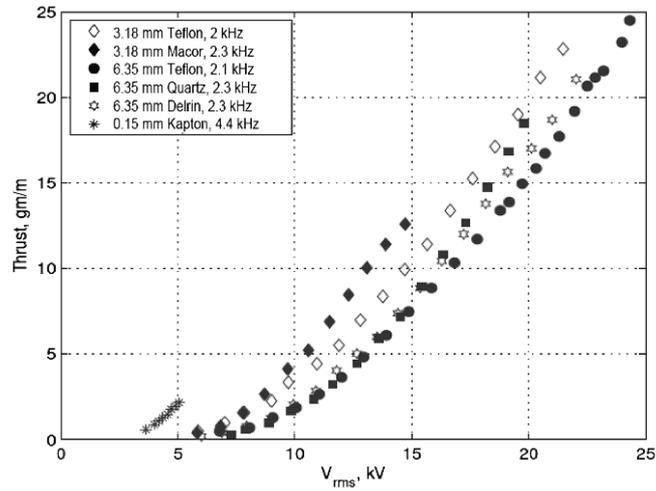
Figure 2.10: Thrust vs applied voltage for different dielectric materials. The thrust is measured by means of a force balance.

Cristofolini et al. [22] investigated the induced EHD flow by means of Schlieren imaging and proved that Teflon dielectrics can support higher flow velocity than Kapton ones, averaged supply power being equal.

CHAPTER 3

MODELLING OF DBD

Se non sai cosa dire, taci.

(Quinto)

Abstract. The chapter presents the 2-species drift diffusive model for plasma kinetics. It is the most widely adopted physical model for DBD and couples 2 drift diffusive model to describe charged species motion with the Poisson equation for the electric field. This rather simple approach is the easiest way to describe a very complex non-equilibrium environment where interactions between highly reactive species with bulk molecules and electrodes introduce a large amount of uncertainty and represent the key factor for a better knowledge and control of DBD.
Even though the discussion is focused on plasma actuators for EHD as this was the original aim of the study, it can be extended to other fields.

Introduction

Modelling of DBD was mainly studied for flow control via EHD interaction. Since the aim is to estimate the body force exerted on the gas by the discharge, it was assumed that 2-species models are accurate enough and characteristics like chemical composition and energy levels of species are not investigated. Knowledge about these aspects is instead necessary to approach medical skin treatments or plasma assited combustion, where chemical reactions are fundamental to generate reactive species which interact with the operating gas or solid material.

A scheme of all the reactions generated by DBD is provided by Solov'ev et al [25] and is displayed in tab. 3.1, showing all phenomena which should be taken into account for studying air-operated EHD.

When operating DBD in a pure gas, the chemical composition is simpler and less species are generated. This is the reason why some authors believe that the 2-species approach is reliable only when the DBD is operated in a pure gas such as nitrogen.

Electron impact

$$e + N_2 \Leftrightarrow 2e + N_2^+$$
$$e + O_2 \Leftrightarrow 2e + O_2^+$$
$$e + O_2 \Leftrightarrow O^- + O$$
$$e + 2O_2 \Leftrightarrow O_2^- + O_2$$
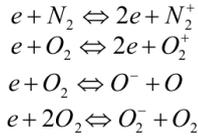
Dissociation reaction

$$e + O_2^+ \Leftrightarrow O + O$$
$$e + O_4^+ \Leftrightarrow O_2 + O_2$$

Exchange reaction

$$O_2^+ + O_2 + O_2 \Leftrightarrow O_4^+ + O_2$$
$$O_2^+ + O_2 + N_2 \Leftrightarrow O_4^+ + N_2$$
$$N_2^+ + N_2 + O_2 \Leftrightarrow N_4^+ + O_2$$
$$N_2^+ + N_2 + N_2 \Leftrightarrow N_4^+ + N_2$$
$$N_4^+ + O_2 \Leftrightarrow 2N_2 + O_2^+$$
$$N_2^+ + O_2 \Leftrightarrow N_2 + O_2^+$$

Thermal dissociation

$$N_4^+ + O_2 \Leftrightarrow N_2^+ + N_2 + O_2$$
$$N_4^+ + N_2 \Leftrightarrow N_2^+ + N_2 + N_2$$
$$O_4^+ + N_2 \Leftrightarrow O_2^+ + O_2 + N_2$$
$$O_4^+ + N_2 \Leftrightarrow O_2^+ + O_2 + N_2$$

Attachment Reaction

$$O^- + O_2 + O_2 \Leftrightarrow O_3^- + O_2$$
$$O^- + O_2 + N_2 \Leftrightarrow O_3^- + N_2$$
$$O^- + N_2 \Leftrightarrow e + N_2O$$
$$A^+ + B^- + O_2 \Leftrightarrow A + B + O_2$$
$$A^+ + B^- + N_2 \Leftrightarrow A + B + O_2$$
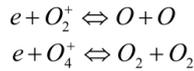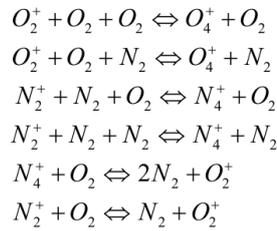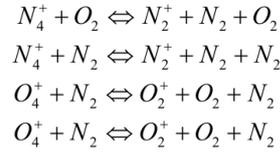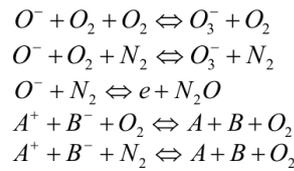
UV radiation (98.0-102.5 nm)

$$N_2(b^1\pi_u, b^{''1}\pi_u, c_4^{'1}\Sigma_u^+)$$
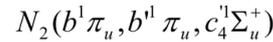
Figure 3.1: Chemical reactions involved in air-operated DBD

3.1   Electrohydrodynamic force: the Drift-Diffusive model

As discussed in the previous chapters, DBD is composed of random microdischarges developing from the cathode to the anode. The characteristic time for microdischarges propagation in the air gap is hundreds of ns and the lenght scale of streamers head is some nm. Comparing this time and lenght scales to characteristic time of AC power supply and size of plasma actuators suggests the extremely detailed numerical resolution required to duplicate every random microdischarge involved in DBD. The approach adopted here is the same proposed by Boeuf [16], who attempted to reproduce the global effect of DBD without simulating single microdischarges.

Fig. 3.2 shows the simplified model interpretation of microdischarge (positive upper electrode) as composed by a globally neutral plasma bulk and a sheat cathode region propagating downstream with respect to the gas flow. The body of the streamer is globally neutral and hence there is no voltage drop inside it: its voltage is the same as the exposed electrode. The sheat region behaves instead like a moving cathode where the voltage drop is concentrated. The discharge is sustained by the Townsend avalanche mechanism introduced in chap. 1.
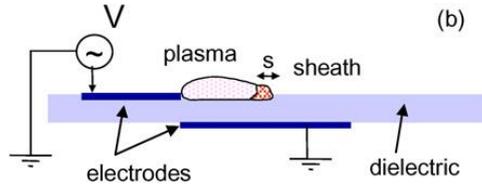

Figure 3.2: Structure of a single streamer channel during the positive voltage half cycle [16]

The body force is due to charged particles collisions with neutrals and the balance to be evaluated is then associated with momentum equations for charged species. Being the mean ionization rate around 10^{-6}, collisions involving only charged particles are negligible with respect to collisions between charged particles and neutrals. Hence, the electron-neutrals collision frequency $\nu_{coll,e}$ and the ion-neutrals collision frequency $\nu_{coll,i}$ are the only considered here. Usual value for these collision frequencies is $10^9 \, Hz$ and it is possible to suppose that local equilibrium is reached for charged particles because $\nu_{coll,e}$ and $\nu_{coll,i}$ are much higher than the AC frequency. This means that the momentum gained because of the E-field is instantaneously and completely lost in collisions with neutrals, in the AC time scale. If the mean velocity u_c of the charged-species c is assumed much higher than the gas flow velocity u_n, then $u_c - u_n = u_c$. The momentum equation for the

charged species c is:

$$n_c \, q_c \, E = \nu_{coll,c} \, n_c \, m_c \, u_c \tag{3.1}$$

where n_c, q_c, m_c and $\nu_{coll,c}$ are respectively the number density, electric charge, mass and collision frequency with neutrals for the c-charged species. The momentum transferred to the bulk gas per unit volume is then $n_c \, q_c \, E$ for the c-species.

The most simple model we used was first introduced by Boeuf [16] and considers only two charged species, electrons and positive ions, so the total net force on the gas has only two components, opposite to one another:

$$\vec{F} = (n_i - n_e)q\vec{E} \tag{3.2}$$

This rather simple equation shows that the EHD force is larger in regions with large electric field or large charge separation, as happens in the sheat cathode region of fig: 3.2 but not in the body of the streamer channel. It also determines the quantities to be calculated to have an estimate of the body force, which are, consequently, the E-field and the charged species number density.

The electric field can be obtained through the Poisson equation (3.3), because there is no time-varying B-field and E is conservative.

$$\nabla^2 \phi = -\frac{\rho_c}{\epsilon} \tag{3.3}$$

Where ϕ is the electric potential and ρ_c the electric charge density, ϵ the dielectric permittivity.

With respect to the charged particles number density, more stricht assumptions need to be made. Continuity equations describe the time evolution of any species according to sources S_c and flux $\vec{\Gamma_c}$:

$$\frac{\partial n_i}{\partial t} = S_i - \nabla \cdot \vec{\Gamma_i} \tag{3.4}$$

$$\frac{\partial n_e}{\partial t} = S_e - \nabla \cdot \vec{\Gamma_e} \tag{3.5}$$

The so-called *Drift-Diffusive* model is the name of the approach used to express the above introduced fluxes, implying that the electric field and number density gradients are responsible for charged particles motion.

$$\vec{\Gamma_i} = n_i \, \mu_i \, \vec{E} - D_i \, \nabla n_i; \tag{3.6}$$

$$\vec{\Gamma_e} = n_e \, \mu_e \, \vec{E} - D_e \, \nabla n_e \tag{3.7}$$

. . . .

where $\mu_c = q_c/m_c\nu_{cn}$ is the electric mobility of the charged species c and D_c is its diffusive coefficient. Sources are also dependent on fluxes, and account for ionization and recombination:

$$S_i = \alpha|\vec{\Gamma}_i| - r_{ei}\,n_e\,n_i; \tag{3.8}$$

$$S_e = \alpha|\vec{\Gamma}_e| - r_{ei}\,n_e\,n_i \tag{3.9}$$

where α is the ionization coefficient and r_{ei} the recombination coefficient. The ionization coefficient is obtained as follows as function of reduced pressure [26]:

$$\alpha = pA\,e^{-B\,p/|\vec{E}|} \tag{3.10}$$

where p is the pressure and A,B are coefficients.

3.2 Boundary conditions

Big uncertainty about all interface phenomena is still present among researchers. However, boundary conditions are essentials to represent key features of dielectric barrier discharge, such as surface charge deposition and secondary electron emission. Thus, simplified assumptions have been considered to approach plasma-wall interactions.
Secondary electron emission is the expulsion of electrons from the cathode surface because of ions collisions. It is represented by the average number of electrons released for every ion collision, γ, and is usually around some percent. Boundary conditions reverse every half AC cycle, so two subsections follow, one for each of them.

Positive exposed electrode

During the positive phase, electrons are attracted by the exposed electrode and positive charges are repelled from it. Secondary electron emission takes place on the dielectric surface and we can assume the only electrons on the cathode are those generated because of this phenomenon, other ones being repelled right away. The boundary conditions on the dielectric for plasma kinetic during the positive voltage half cycle is then:

$$\Gamma_e = \gamma_d\,\Gamma_i \tag{3.11}$$

Positive ions are instead repelled form the anode, so vanishing ions number density is assumed on the upper electrode:

$$n_i = 0 \tag{3.12}$$

Charge accumulation needs also to be considered on the dielectric. Instantaneous recombination for electric charges is assumed on the surface, so the difference $n_i(x,y,t) - n_e(x,y,t)$ gives the instantaneupus local surface charge density $\sigma_c(x,y,t)$ and determines discontinuity in the electrical displacement D_j:

$$\nabla D \cdot \hat{s} = \sigma_c \qquad (3.13)$$

where $\hat{s}$ is the unit vector normal to the surface. Indicating the applied voltage with $V(t)$ and the electric potential with ϕ, the electric boundary condition for the upper electrode during the positive phase is:

$$\phi = V_a \, sin(\omega t) \qquad (3.14)$$

Negative exposed electrode

Ions are attracted by the exposed electrode and electrons are repelled from it when the applied voltage is negative. Secondary emission occurs on the exposed electrode and the relative boundary relation for plasma kinetic follows,

$$\Gamma_e = \gamma_{Cu} \Gamma_i \qquad (3.15)$$

Electrons are pushed away from the cathode so it is assumed that the electron number density vanishes:

$$n_e = 0 \qquad (3.16)$$

With respect to the electric potential, boundary conditions on the dielectric surface still account for charge accumulation:

$$\nabla D \cdot \hat{s} = \sigma_c \qquad (3.17)$$

and the boundary condition for the exposed electrode also doesn't change

$$\phi = V_a \, sin(\omega t) \qquad (3.18)$$

3.3 Numerical Model

The numerical approach proposed in this work was first developed by Dr. G. Huang and Dr. J. Shang form Wright State University of Dayton Ohio [26, 27, 28]. The code was modified to simulate the effect of the dielectric material on discharge properties as well as the body force of DBD. An iterative relaxation procedure (SOR) is selected to solve the numerical problem, which is obtained by discretizing the governing equations (3.3),(3.4),(3.5) according to the finite difference method. These equations are solved indipendently,

so the electric field is evaluated at each time step uncoupled from the conti-
nuity equations and once it is obtained, species concentrations are calculated.

Uncoupling the electrostatic from the plasma kinetic is possible because of
different characteristic times. Characteristic time for DBD is given by the
AC frequency,

$$f_{AC} = 5\,kHz \Rightarrow t_{AC} = f_{AC}^{-1} = 2\cdot 10^{-4}s \tag{3.19}$$

and t_{AC} is the AC period. The electric response of the plasma to external
excitment (AC power) is due to charged particle motion and can then be
characterized by the drift velocity of the species which carry the most electric
current i.e. electrons:

$$v_{drift,e} = \mu_e \vec{E} = \mu_e \frac{\partial V}{\partial x} \Rightarrow t_{drift,e} = v_{drift,e}^{-1} \approx 2.4\cdot 10^{-8}\,s \tag{3.20}$$

Being t_{AC} considerably smaller than $t_{drift,e}$, it is possible to think the charged
particles to react instantaneously to the power supply and the electrostatic
can be studied independently form charged particles motion and generation.

The governing equations can be cast into a flux vector from if the electric
field time derivative is neglected:

$$\frac{\partial \vec{U}}{\partial t} + \frac{\partial \vec{F}_x(\vec{U})}{\partial x} + \frac{\partial \vec{F}_y(\vec{U})}{\partial y} = \frac{\partial \vec{G}_x(\vec{U})}{\partial x} + \frac{\partial \vec{G}_y(\vec{U})}{\partial y} + \vec{S} \tag{3.21}$$

very similar to 2D Euler equations which can be approached with usual
fluid dyanmic methods. The conservative variables vector is:

$$\vec{U} = [\phi,\, n_i,\, n_e], \tag{3.22}$$

the flux vector components are:

$$\vec{F}_x(\vec{U}) = \big[0,\, -\mu_e n_e E_x,\, \mu_i n_i E_x\big], \tag{3.23}$$

$$\vec{F}_y(\vec{U}) = \big[0,\, -\mu_e n_e E_y,\, \mu_i n_i E_y\big], \tag{3.24}$$

$$\vec{G}_x(\vec{U}) = \left[\frac{\partial \phi}{\partial x},\, D_e \frac{\partial n_e}{\partial x},\, D_i \frac{\partial n_i}{\partial x}\right], \tag{3.25}$$

$$\vec{G}_y(\vec{U}) = \left[\frac{\partial \phi}{\partial y},\, D_e \frac{\partial n_e}{\partial y},\, D_i \frac{\partial n_i}{\partial y}\right], \tag{3.26}$$

and

$$\vec{S} = [-\frac{n_i - n_e}{\epsilon},\, \alpha|\vec{\Gamma}_e| - \beta n_i n_e,\, \alpha|\vec{\Gamma}_e| - \beta n_i n_e] \tag{3.27}$$

is the source term. As previously stated, this formulation is good for classical fluid dynamics approaches and it is to be stressed that no equation involving time derivatives of the electric field is solved.

The *delta formulation* is adopted to take the difference of dependent variables in consecutive iteration levels, $\Delta \vec{U} = \vec{U}^{n+1} - \vec{U}^n$, which is achieved by flux vector linearization as an approximate Riemann problem. The steady state formulation of eq. (3.21) is then evaluated at every time step.

$$\Delta \vec{F}_x = \vec{F}_x^{n+1} - \vec{F}_x^n \approx \vec{A}_x^n \Delta \vec{U}, \tag{3.28}$$

$$\Delta \vec{F}_y = \vec{F}_y^{n+1} - \vec{F}_y^n \approx \vec{A}_y^n \Delta \vec{U}, \tag{3.29}$$

$$\Delta \vec{G}_x = \vec{G}_x^{n+1} - \vec{G}_x^n \approx \vec{B}^n \frac{\partial \Delta \vec{U}}{\partial x}, \tag{3.30}$$

$$\Delta \vec{G}_y = \vec{G}_y^{n+1} - \vec{G}_y^n \approx \vec{B}^n \frac{\partial \Delta \vec{U}}{\partial y}, \tag{3.31}$$

having defined n the iteration level and

$$A_x = \frac{\partial \vec{F}_x}{\partial \vec{U}} = \Lambda\big[0, -\mu_e E_x, \mu_i E_x\big], \tag{3.32}$$

$$A_y = \frac{\partial \vec{F}_y}{\partial \vec{U}} = \Lambda\big[0, -\mu_e E_y, \mu_i E_y\big], \tag{3.33}$$

$$B = \frac{\partial \vec{G}_x}{\partial \vec{U}} = \frac{\partial \vec{G}_x}{\partial \vec{U}} = \Lambda\big[1, D_e, D_i\big]. \tag{3.34}$$

It must be noted that this formulation gives uncoupled equations which can be solved separately in a sequential manner. Applying the iterative relaxation procedure for the generic time level implies dropping the time derivative term and substituting eq.s (3.28),(3.32) in eq. (3.21) to get:

$$\frac{\partial \Delta \vec{F}_x}{\partial x} + \frac{\partial \Delta \vec{F}_y}{\partial y} = \frac{\partial \Delta \vec{G}_x}{\partial x} + \frac{\partial \Delta \vec{G}_y}{\partial y} + \vec{R}^n \tag{3.35}$$

where

$$\vec{R}^n = -\frac{\partial \vec{F}_x^n}{\partial x} - \frac{\partial \vec{F}_y^n}{\partial y} + \frac{\partial \vec{G}_x^n}{\partial x} + -\frac{\partial \vec{G}_y^n}{\partial y} + \vec{S}^n \tag{3.36}$$

Convergence is achieved for $\vec{R}^n \to 0$ which means eq. (3.21) to be satisfied and solution for the generic time level reached.

The right hand side of eq. (3.35) is explicit and can be evaluated with any numerically stable differencing scheme. Two different schemes for diffusive

and convective terms are adopted.

Diffusive and source terms were discrtized using a central scheme:

$$\frac{\partial \vec{G}_x^n}{\partial x} \approx \frac{\vec{G}_{x_{i+1/2,j}}^n - \vec{G}_{x_{i-1/2,j}}^n}{x_{i+1/2} - x_{i-1/2}}, \tag{3.37}$$

where

$$\vec{G}_{x_{i+1/2,j}}^n = B\left(\frac{\partial \vec{U}}{\partial x}\right)_{i+1/2,j}^n = B\frac{\vec{U}_{i+1,j}^n - \vec{U}_{i,j}^n}{x_{i+1} - x_i}. \tag{3.38}$$

A high order upwind scheme is employed for convective fluxes. The flux $\vec{F}_x^n$, for example, is treated as follows:

$$\frac{\partial \vec{F}_x^n}{\partial x} \approx \frac{\vec{F}_{x_{i+1/2,j}}^n - \vec{F}_{x_{i-1/2,j}}^n}{x_{i+1/2} - x_{i-1/2}}, \tag{3.39}$$

where

$$\vec{F}_{x_{i+1/2,j}}^n = \frac{1}{2} A_{x_{i+1/2,j}}^n \left(\vec{U}_{R_{i+1/2,j}}^n + \vec{U}_{L_{i+1/2,j}}^n\right)$$
$$- \frac{1}{2}|A_{x_{i+1/2,j}}^n|\left(\vec{U}_{R_{i+1/2,j}}^n - \vec{U}_{L_{i+1/2,j}}^n\right). \tag{3.40}$$

The subscript R and L indicate the upwind interpolation for the right and left sides, respectively. A quadratic Lagrange interpolation is used, so that $U_{R_{i+1/2,j}}^n$ is obtained considering nodal values of the independent variable $\vec{U}$ at nodal locations (x_i, y_j), (x_{i+1}, y_j), (x_{i+2}, y_j) and $U_{L_{i+1/2,j}}^n$ is evaluated from (x_{i-1}, y_j), (x_i, y_j), (x_{i+1}, y_j).

The left hand side of eq. (3.35) is implicit instead. A central differential scheme identical to (3.37) is used for diffusive terms of $\Delta \vec{U}$. The convective terms are discretized by a first order upwind scheme to ensure numerical stability.

$$\frac{\partial \Delta \vec{F}_x}{\partial x} \approx \frac{\Delta \vec{F}_{x_{i+1/2,j}} - \Delta \vec{F}_{x_{i-1/2,j}}}{x_{i+1/2} - x_{i-1/2}}, \tag{3.41}$$

where

$$\Delta \vec{F}_{x_{i+1/2,j}} = \frac{1}{2} A_{x_{i+1/2,j}}^n \left(\Delta \vec{U}_{i+1,j} + \Delta \vec{U}_{i,j}\right)$$
$$- \frac{1}{2}|A_{x_{i+1/2,j}}^n|\left(\Delta \vec{U}_{i+1,j} - \Delta \vec{U}_{i,j}\right). \tag{3.42}$$

Eq. (3.35) can be written as a function of the only independent variable vector $\Delta \vec{U}$:

$$
\begin{aligned}
a_{i,j}\Delta \vec{U}_{i,j} = a_{i+1,j}\Delta \vec{U}_{i+1,j} + a_{i-1,j}\Delta \vec{U}_{i-1,j} \\
+ a_{i,j+1}\Delta \vec{U}_{i,j+1} + a_{i,j-1}\Delta \vec{U}_{i,j-1} + R^n \quad (3.43)
\end{aligned}
$$

where R^n is defined by eq. (3.36) and the matrix coefficients a are defined:

$$
\begin{aligned}
a_{i+1,j} &= \frac{\frac{1}{2}\left(|A^n_{x_{i+1/2,j}}| - A^n_{x_{i+1/2,j}}\right)}{x_{i+1/2} - x_{i-1/2}} + \frac{B}{(x_{i+1} - x_i)(x_{i+1/2} - x_{i-1/2})} \\
a_{i-1,j} &= \frac{\frac{1}{2}\left(|A^n_{x_{i-1/2,j}}| + A^n_{x_{i-1/2,j}}\right)}{x_{i+1/2} - x_{i-1/2}} + \frac{B}{(x_i - x_{i-1})(x_{i+1/2} - x_{i-1/2})} \\
a_{i,j+1} &= \frac{\frac{1}{2}\left(|A^n_{y_{i,j+1/2}}| - A^n_{y_{i,j+1/2}}\right)}{y_{j+1/2} - y_{j-1/2}} + \frac{B}{(y_{j+1} - y_j)(y_{j+1/2} - y_{j-1/2})} \\
a_{i,j-1} &= \frac{\frac{1}{2}\left(|A^n_{y_{i,j-1/2}}| + A^n_{y_{i,j-1/2}}\right)}{y_{j+1/2} - y_{j-1/2}} + \frac{B}{(y_j - y_{j-1})(y_{j+1/2} - y_{j-1/2})} \\
a_{i,j} &= a_{i+1,j} + a_{i-1,j} + a_{i,j+1} + a_{i,j-1} + q \\
q &= \frac{A^n_{x_{i+1/2,j}}}{x_{i+1/2} - x_{i-1/2}} - \frac{A^n_{x_{i-1/2,j}}}{x_{i+1/2} - x_{i-1/2}} + \frac{A^n_{y_{i,j+1/2}}}{y_{j+1/2} - y_{j-1/2}} - \frac{A^n_{y_{i,j-1/2}}}{y_{j+1/2} - y_{j-1/2}}.
\end{aligned}
$$
$$(3.44)$$

The 2D computational domain in use is shown in fig. 3.3. A rectangular grid suitable for finite difference method is studied for bith the electrostatics and plasma kinetics. Geometric progression is adopted to refine the mesh near electrodes and the dielectric surface, in order to catch the fundamental physical properties where gradients are large. The most critical point is the upper right corner of the exposed electrode because electric field gradient is enhanced by sharpness. The dielectric is assumed $1\,mm$ thick and the electrode above it is $6\,mm$ wide x-wise, while the embedded one is $13\,mm$ wide; both of them have the same thickness of $0.1\,mm$. The origin of axes is placed at the left intersection corner between the exposed electrode and the dielectric surface. No x-gap between electrodes is considered. The following image fig. 3.4 displays electrodes ad dielectric position in the mesh system.
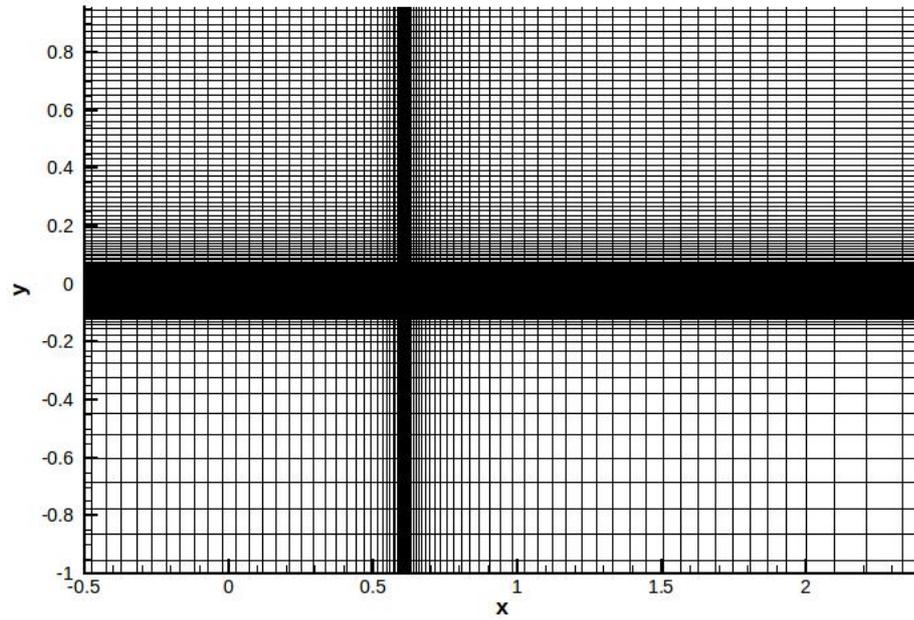
**Figure 3.3:** Computational domain with strong refinement near electrodes and dielectric surface.
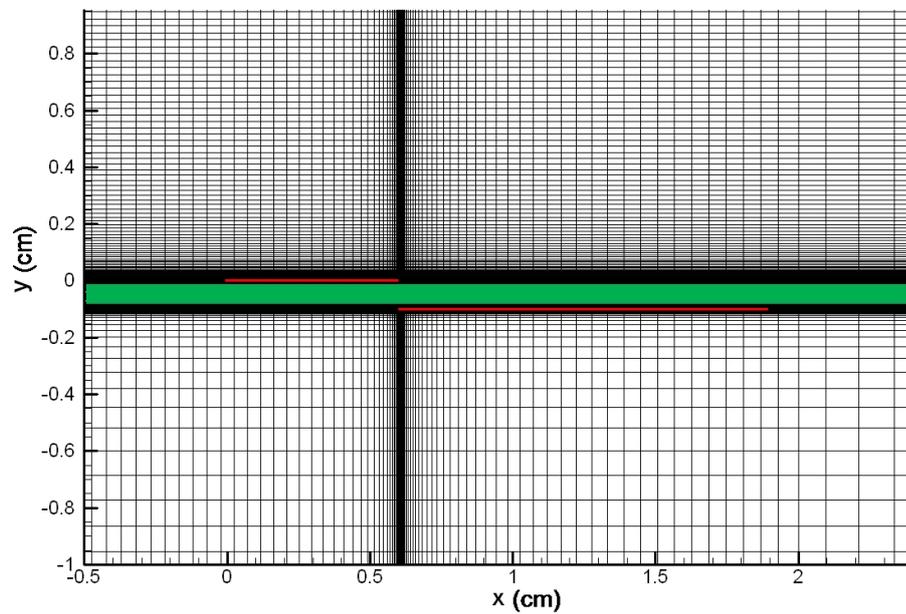
Figure 3.4: Computational domain with electrodes (red) and dielectric barrier (green).

DBD AND EHD SIMULATION RESULTS

Non ci sono piú i figli di una volta.
(Mansueta)

Abstract. This chapter presents the simulation results about the DBD according to the code introduced in the previous chapter. Calculations provide estimation of the effect of the dielectric material and of the applied voltage on the discharge properties and quantify the averaged body force over an AC cycle.
In the second part of the chapter, EHD simulation results according to a modified OpenFOAM opensource software are discussed.
Finally, numerical validation of experimental results on Shlieren investigations of DBD is presented.

Introduction

The numerical model introduced in chapter 3 was implemented to simulate
the discharge evolution in time. Fig. 4.1 includes an example of both V vs
time and I vs *time* plots for DBD calculations, where I is the total current,
composed of displacement and conductive current. $10\,kHz$ AC frequency and
maximum applied voltage of $3\,kV$ were assumed. Three different grid sys-
tems (192×302; 382×602; 762×1202) are compared in the figure to show
how brakdown and electric parameters vary according to mesh refinement.
From the figure the typical discharge pattern can be understood.
When the breakdown voltage is reached, conductive current flows across the
gas. Nevertheless, major spikes in the total current plot are due to electric
potential surge at breakdown, causing intense generation of displacement
current. During the positive phase, the conductive current is consistenly
negative, which means it is directed towards the exposed electrode and re-
verses during the negative phase. On the other hand, displacement current
follows temporal derivative of the electric potential, being positive when the
voltage is increasing and negative otherwise. The maximum magnitude of
the total current is larger in the negative phase and is about $1\,mA/cm$.
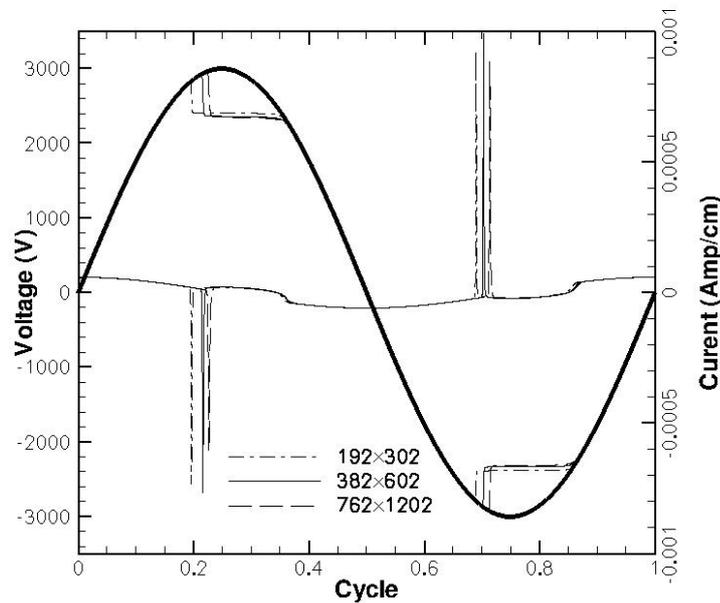
Figure 4.1: Dicharge voltage and total current over one AC
period. Current unit is per *cm* depth in the z-direction

These results have been validated in several works by Shang et al. and prove

to be globally consistent [26, 27]. For example, fig. 4.2 shows that the drift diffusion model and the numerical formulation introduced above, effectively describes and represents a meaningful feature of DBD. Photos on the right side are taken from Hoskinson [29] and portray the discharge structure when the applied voltage is positive ($\varphi > 0$, top) and negative ($\varphi < 0$, bottom) propagating from left to right. Comparing these photos with pictures from simulations, on the left side for the same AC phases, proves that the drift diffusion model effectively duplicate the further propagation of the discharge during the positive rather than during the negative half-period, even though single streamers and microdischarges propagation is not duplicated.
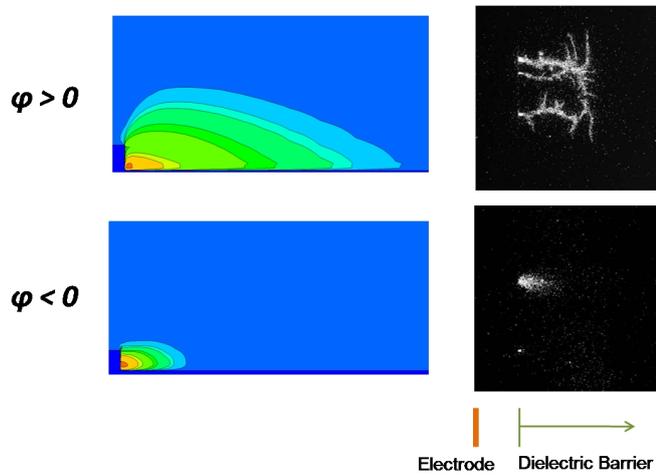

Figure 4.2: Drift-diffusion model validation: comparison between results and photos form above the dielectic surface.

4.1   Dielectric material

The first simulation campaign was undertaken to understand the effect of the dielectric material on the discharge properties. Three different values of the dielectric constant have been used for comparisons: $\epsilon = 2.7$ for Teflon, $\epsilon = 4.7$ for plexiglass and $\epsilon = 6.7$ for glass.
The breakdown voltage is deeply affected by the value of ϵ because it determines the amount of charge to separate in order to achieve a given electric potential. Before breakdown, when there is no charge separation in the gas gap, increasing the dielectric permittivity leads to higher electric displacment and hence to higher electric field in the gas: higher values of dielectric permittivity imply that the brakdown electric field in the gas is obtained for lower values of the externally applied voltage. This effect also determines longer discharge duration for higher values of the dielectric constant.

Fig. 4.3 depicts this dependence for applied voltage of $4\,kV_{pp}$, $f_{AC} = 5\,kHz$ and shows that the code effectively catches the abovementioned behavior. As the dielectric constant is changed from Teflon ($\epsilon = 2.7$) to plexiglass ($\epsilon = 4.7$) the brakdown voltage lowers from $3.6\,kV$ to $3.2\,kV$. Slighter decrease shows lowering the value of ϵ for glass ($\epsilon = 6.7$).
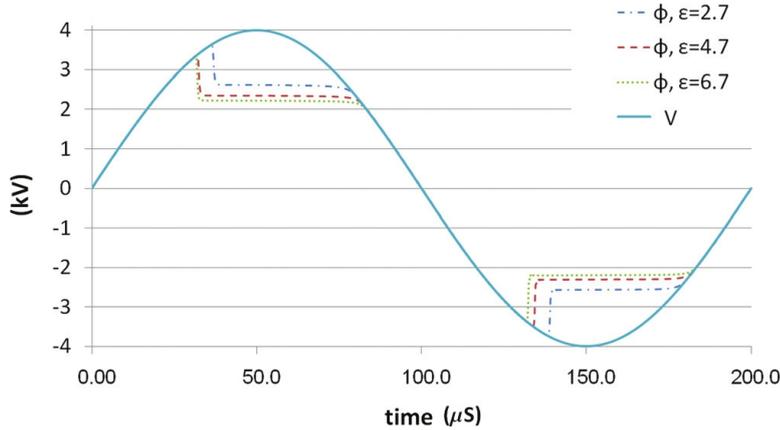

Figure 4.3: Breakdown voltage and discharge duration for different dielectric materials.

The discharge time evolution was also compared for different permittivity of the dielectric material. Fig. 4.4 portrays the discharge area at different time steps. The upper part of the picture compares ion number densities for teflon ($\epsilon = 2.7$) and glass ($\epsilon = 6.7$). Only ion number density is displayed because the large difference in electric mobility between electrons and ions makes the seconds heavily outnumber the firsts.

The discharge domain is much larger if the permittivity is lower because ions are subject to lower electric field and can propagate further. Nevertheless, Higher ionization rate is achieved for higher values of ϵ, up to $10^{12}\,cm^{-3}$ for $\epsilon = 6.7$ in the very recess corner between the exposed electrode and the dielectric barrier.

A similar behavior generates when the exposed electrode acts as cathode. It must be noted that this representation also describes lower breakdown voltage for greater electric permittivity, leading to longer discharge duration.

The discharge current was also studied in both its componenets, the displacement and the conductive one. The top picture of fig. 4.5 shows the conductive current intensity has a surge at breakdown and then smoothly follows the external voltage until the discharge is ceased. This current component is increased by higher values of ϵ and there is a larger difference between Teflon and plexiglass rather than between plexiglass and glass. This effect is consistent with numerical results displayed for breakdown voltage and greater electric field achieved for higher values of the dielectric permit-
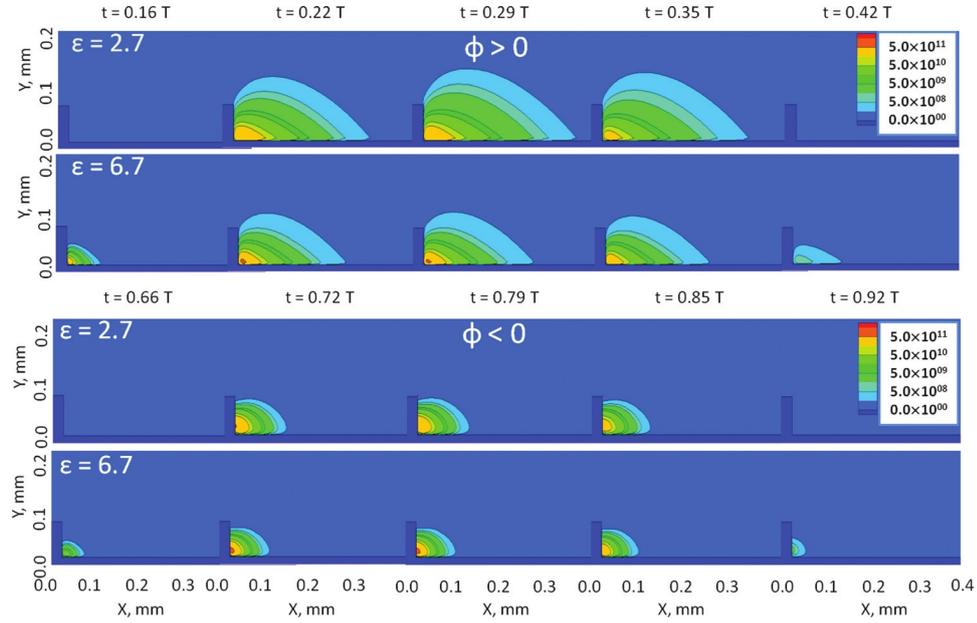
Figure 4.4: Discharge evolution for the positive (top) and the negative phase (bottom) compared for different values of ϵ. The discharge area is shown at different time levels (T indicates the AC period).

tivity.

The bottom picture of fig. 4.5 depicts the effect of the dielectric material on the displacement current according to the drift-diffusion model. The displacement current has a peak of some mA/cm at breakdown when the electric displacment D has an abrupt variation; for different times the value of the displacement current is much lower and follows the applied voltage. Again, higher values of the dielectric permittivity are responsible for higher values of the electric field and then greater variations of the electric displacement, resulting in higher displacement current intensity.

4.2   Applied voltage

The externally applied voltage influence on discharge properties was studied. Fig. 4.6 portrays the effect of the external voltage (EMF in the picture) on the breakdown voltage and discharge duration. Increasing the value of EMF from $4kV$ to $8kV$ leads to sooner breakdown because the critical electric field is achieved sooner and thus a longer discharge duration is obtained. The discharge lasts for 66% of the AC period for $4kV$ and for 78% for $8kV$ calculations.

. . . .
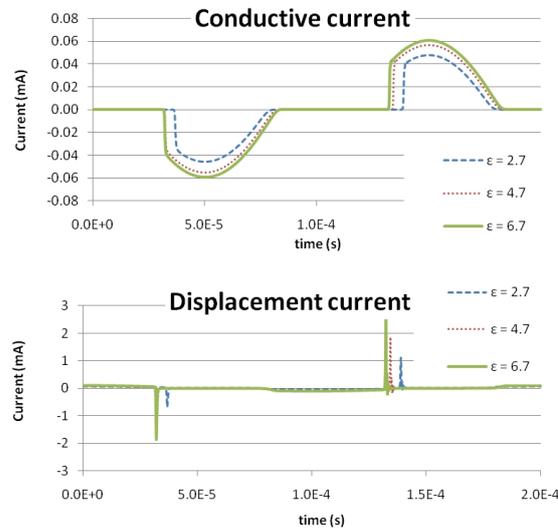
Figure 4.5: Conductive (top) and displacement current (bottom) for different dielectric materials
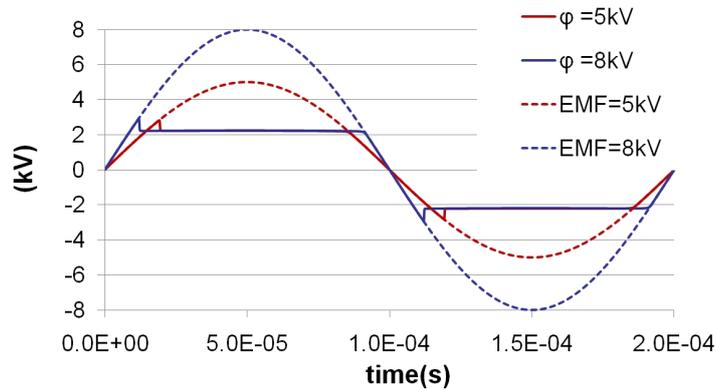

Figure 4.6: Breakdown voltage comparison for different amplitude of the applied voltage.

The ion cloud maximum extent for different values of the applied voltage is shown in fig. 4.7. The dischare region and the maximum ionization rate are increased by increasing the applied voltage.

As well as the dielectric material, the applied voltage too affects the discharge current intensity and fig. 4.8 shows the displacement current intensity is roughly increased of 40% its peak value changing the applied voltage from 5 to 8 kV.
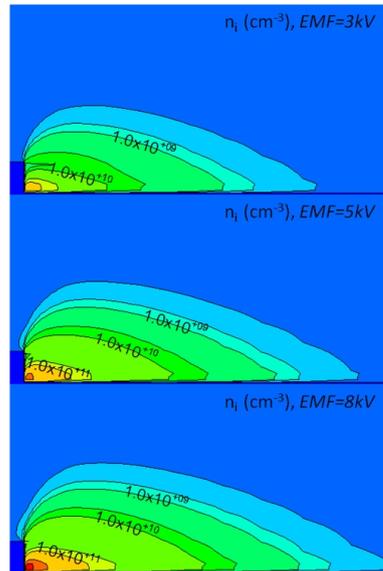
Figure 4.7: Discharge domain and ion concentration for different values of the applied voltage. In each case, pictures are taken for positive peak values of the applied voltage.
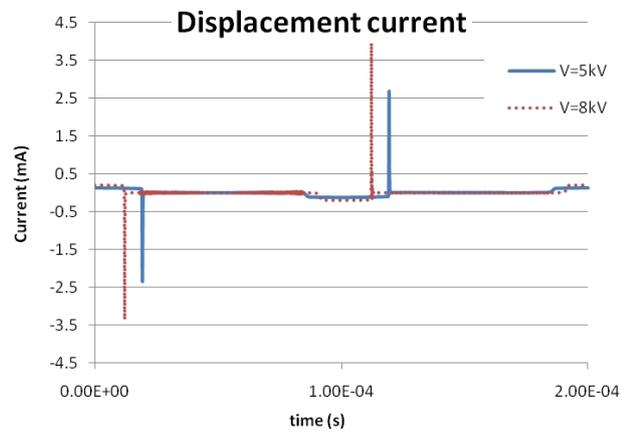

Figure 4.8: Displacement current comparison for different values of the external voltage amplitude.

4.3 ElectroHydroDynamic force

Sampled instantaneous force

The interaction between the bulk gas and the discharge is due to momentum transfer from charged particles to neutrals. It is then the force balance for the unit volume which quantifies this interaction.
The two components of the electrodynamic force are:

$$f_x(x, y, t) = -q(n_i - n_e)\frac{\partial \phi}{\partial x}, \tag{4.1}$$

$$f_y(x, y, t) = -q(n_i - n_e)\frac{\partial \phi}{\partial y}. \tag{4.2}$$

These quantities have been calculated at each time step. Fig. 4.9 shows the sampled instantaneous x-force over an AC cycle for 3 different locations when the amplitude of the applied voltage is $8\,kV$ and AC frequency is $5\,kHz$ (AC period T lasting $200\,\mu s$). These locations have the same x-distance from the exposed electrode of $6\,\mu m$. The plot describes quite interesting features of the electrodynamic force according to the drift diffusion model. First of all, it states that the force direction reverses during each half cycle. Second, it shows that the location where the maximum magnitude of the electrodynamic force is reached during the postive phase is not the same where the maximum magnitude of the force is achieved during the negative phase (the blue line has greater magnitude than the red line for $V < 0$ but lower for $V > 0$). Third, the magnitude of the instantaneous force can be as high as $2.0 \cdot 10^5\,dyn/cm^3$ ($20\,MN/m^3$), large enough to considerably modify boundary layer fluid dynamic properties. Finally the plot shows that the EHD force is exerted in a very small region close to the recess corner between the exposed electrode and the dielectric surface, its intensity decreasing greatly far from it. Figure. 4.10 displays sampling locations for the positive and the negative phase with the ion cloud taken at its maximum extent in each phase.

Fig. 4.11 also shows the sampled instantaneous x-force over an AC period for different locations when the amplitude of the applied voltage is $8\,kV$. In this second case, the locations have the same height above the dielectric surface of $25\,\mu m$. The plot confirms results from the previous discussion, implying the electrodynamic force being concentrated in a really small area close to the intersection between the electrode and the dielectric barrier. Figure. 4.12 displays sampling locations for the positive and the negative phase with the ion cloud taken at its maximum extent in each phase.

The instantaneous y force has not been investigated in detail and it is only possible to predict that its time evolution shoul follow the x component and be about one order magnitude smaller.
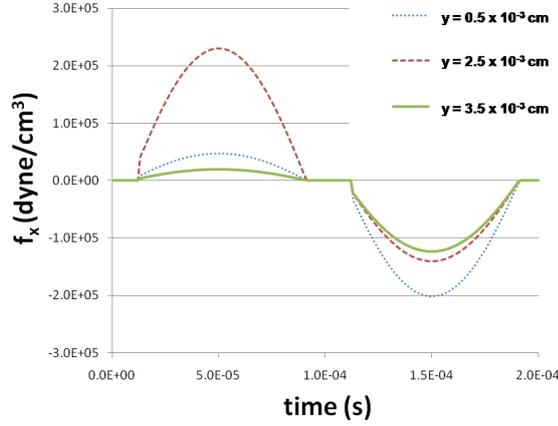
Figure 4.9: Sampled instantaneous x-force for different heights above the dielectric ($6\,\mu m$ x-distance from the exposed electrode).

Time averaged EHD force

As discussed in the previous paragraph, the EHD force was calculated for each location of the computational domain, at every time step. Time averaged EHD force over an AC period was also calulated for every location and a comparison between the maximum magnitude of the instantaneous x-force and the maximum value of the time averaged x-force is shown in fig. 4.13, having defined the maximum instantaneous x-force:

$$\max_{(x,y,t)\in(A\cup T)} f_x(x,y,t). \tag{4.3}$$

and the maximum time averaged x-force:

$$\max_{(x,y)\in A} \bar{f}_x(x,y) = \max_{(x,y)\in A} \frac{1}{T}\int_0^T f_x(x,y,t)\,dt, \tag{4.4}$$

where A is the computational domain. It can be seen how the maximum time averaged force (red line) is much lower than the maximum instantaneous force (blue line), about one order magnitude lower. This plot makes also possible to understand the effect of the externally applied voltage on the EHD force, which is not negligible at all. In particular, changing the value of EMF from $4\,kV$ to $8\,kV$ enhances the momentum transfer and increases the thrust of about ten times. It should be noted that the time averaged force increases with the applied voltage both because the instantaneous force is larger for higer values of EMF and because the discharge lasts for longer if the voltage amplitude is greater.

....

Ion cloud at t = 5x10⁻⁵ s (φ > 0)

Ion cloud at t = 15x10⁻⁵ s (φ < 0)
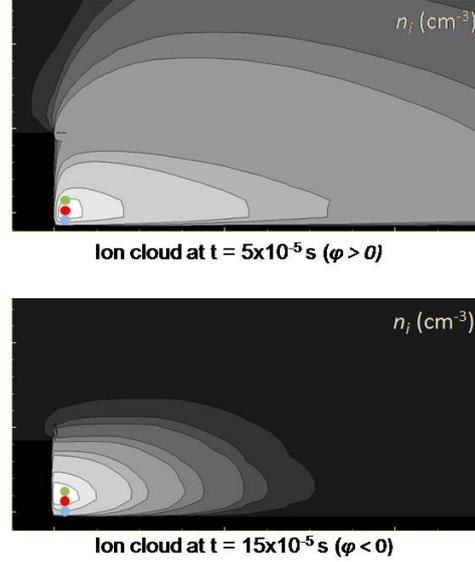
Figure 4.10: Locations for instantaneous x-force sampling. The maximum extent of the ion cloud is also displayed for the positively biased half period (top) and negativly biased one (bottom).

Time and space averaged EHD force

The final evaluation from the plasma kinetics code involved time-space average of the EHD force instantaneous values. In order to perform a space average, a reference domain had to be estabilished. It was chosen to consider the region where the ionization rate i_r is at least 1% of the maximum ionization rate $i_{r,max}$ achieved throughout the computational domain over the whole AC period. Defining this region $R \mid \forall (x,y) \in R, i_r(x,y) \geq 0.01\, i_{r,max}$, the time space averaged force is defined as follows:

$$\bar{F}_x = \frac{1}{T} \int_0^T \frac{1}{A_R} \iint_R f_x(x,y,t)\, dt\, da_r; \tag{4.5}$$

$$\bar{F}_y = \frac{1}{T} \int_0^T \frac{1}{A_R} \iint_R f_y(x,y,t)\, dt\, da_r. \tag{4.6}$$

where A_R is the area of the region R.

Fig. 4.14 portrays the time space averaged force for different values of the applied voltage, green line being the y-force and the red being the x-force. The global behavior is of pushing towards the dielectric barrier ($f_y < 0$) and away from the exposed electrode ($f_x > 0$) and this is in agreement with experiments which show the *electric wind* flowing downstream with respect
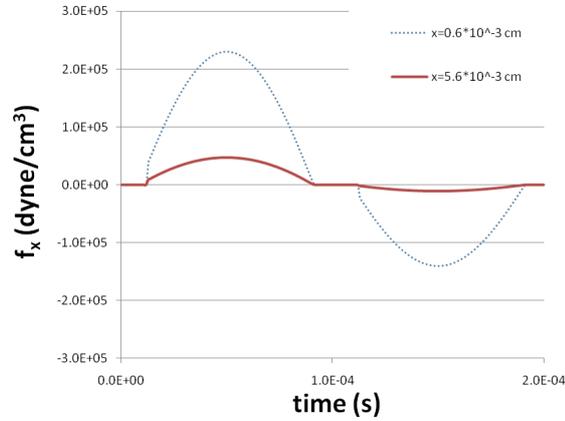
Figure 4.11: Sampled instantaneous x-force for different distances from the exposed electrode ($y = 25\,\mu m$).

to a superimposed flow coming from the exposed electrode. This also means that even though the instantaneous electrodynamic force can be negative (fig. 4.9) and a suction towards the exposed electrode may generate, the overall effect is balanced.

The average magnitude is increased by increasing the applied voltage but the values are small compared to the instantaneous force, about three order magnitude lower, being the time-space averaged EHD force for $8\,kV$ calculations as high as $100\,dyn/cm^3$ ($1\,kN/m^3$). A further element must be taken into account when investigating the effect of the applied voltage. If the external voltage amplitude is increased, the discharge region A_R where ionization is considerable is larger. This implies a larger area where the force is exerted and the global thrust experienced by the fluid is greater also, both because of the more intense force and of the larger area where the force is applied.

Considering the characteristic time of electric response much shorter than fluid dynamic characteristic time (as discussed in the following paragraph) this values can legitemately be assumed as the only momentum source *felt* by the bulk gas.

The blue line in fig. 4.14 describes the variation of the x-force averaged during the positive half cycle only, so the negative effects of opposite thrust during the negative phase are avoided. It can be seen how rectifying the applied voltage could definitely increase the net force transferred to the fluid, but this is only virtually possible. In fact, DBD needs alternative power supply to operate; this curve represents just the positive effect which is partially vanished during the negative phase, according to the proposed model.

. . . .
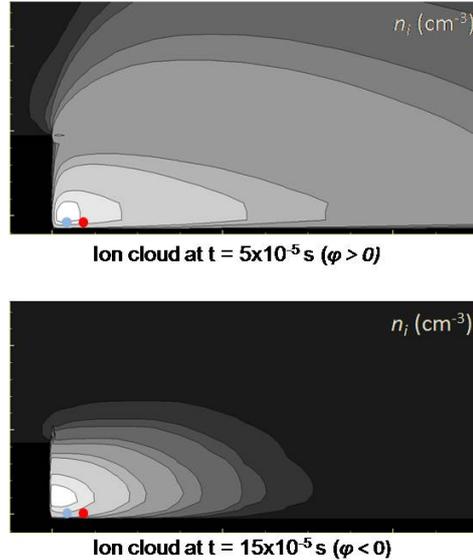
Figure 4.12: Locations for instantaneous x-force sampling. The maximum extent of the ion cloud is also displayed for the positively biased half period (top) and negativly biased one (bottom).

4.4 EHD simulations: OpenFOAM

The $C++$ opensource software *OpenFOAM* provides a variety of free solvers for fluid dynamic simulations, suitable for many case studies. The unstationary compressible solver *rhoPisoFoam* was modified for EHD calculations. The source code was changed to account for both the thrust and the heating effect introduced by the plasma actuator.

The body force obtained and described in the previous paragraph 4.3 for $8\,kV$ calculations is added to the transient 3D solver as well as the heating effects due to ohmic dissipation. Heating effects are experimentally evaluated by measuring the active power supplied to the plasma actuator.
The gas was air, initially at rest. It was assumed the body force magnitude to be as high as $1.69\,N\!/m^3$ and two equally great components of the EHD force were distributed over an area of $1 \cdot 10^{-9}\,m^3$. Ohmic dissipation supplies about $0.1\,MW\!/m^3$ to the gas in the discharge region. $293\,K$ constant wall temperature was imposed while zero gradient boundary conditions for the temperature were implemented for the other borders.
Nevertheless, results were discouraging. The implemented body force was not strong enough for inducing considerable velocity to the flow. This means that the way of implementing the drift diffusion model adopted does not ef-
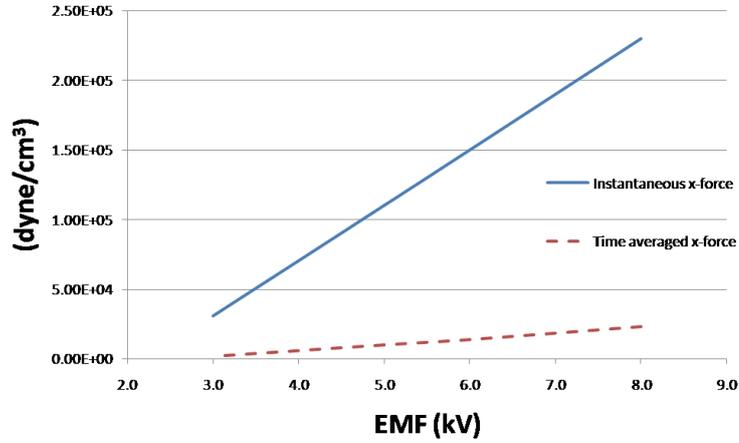
Figure 4.13: Maximum magnitude of the instantaneous x-force and of the time averaged x-force for different values of the applied voltage.
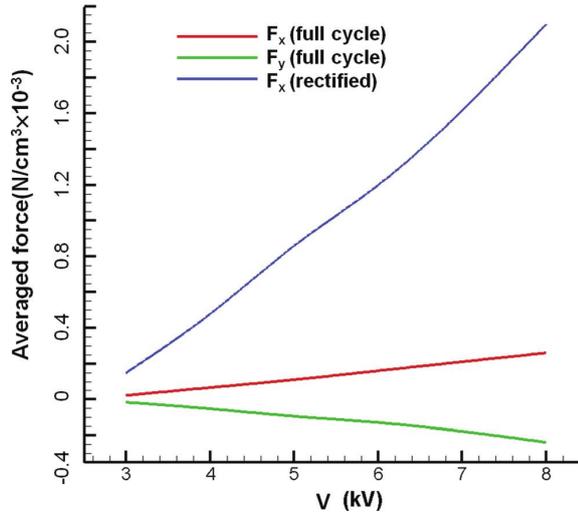

Figure 4.14: Time-Space averaged EHD force at different values of the applied voltage.

fectively reproduce the real effect of the EHD interaction. Even though some features of dielectric barrier discharge are caught by the described simplified approach, it fails in describing the most important characteristic for aerodynamics applications, i.e. the body force. It is thus necessary to develop a numerical way to follow step by step microdischarges evolution.

The negative results obatined from this part of the work led to investigate the appropriate form of the body force indirectly, by finding the EHD force features which guarantee the best duplication of experimental results.

4.4.1 Inverse investigation on the EHD force

The body force was tuned to duplicate the experimental results achieved by our research group over the last ten years [7],[22]. Measurements obtained with the Pitot tube technique provide informations about EHD induced flow and were taken as reference for the comparison. EHD force magnitude and direction as well as shape and size of the discharge area were considered in this study.
The fluid dynamic computational domain is set larger than the plasma kinetiks one, having x-span of $0.25\,m$ and y-span of $0.08\,m$.
On the basis of unaided eye observation, the x-span of the discharge domain was set $5\,mm$ wide and the y-span was taken as high as the electrode, $0.1\,mm$ thick.
The x-component of the force was set to $6.39 \cdot 10^4\,N/m^3$ and the y-component was $-3,19 \cdot 10^4\,N/m^3$; they were evenly distributed over the discharge domain.
The resulting force density applied to the gas is one order greater than the one obtained from DBD calculations but the discharge area is much larger, being about 1000 times greater than the calculated one. This leads to net global force of $5 \cdot 10^{-5}\,N$ applied to the fluid, 10^5 times greater than plasma kinetic simulation results.
This setting for the EHD force was found to provide meaningful results which well agree with measurements.

Figg. 4.15, 4.16, 4.17, 4.18 display the simulated plasma actuator starting transient at 4 time steps. actuator. Velocity and temperature maps are included. Line plots are also shown reporting the x-component of the flow velocity as a function of the height above the dielectric surface, for a x-distance of 1, 3, $6\,cm$ from the exposed electrode. The corner between the exposed electrode and the dielectric surface is located at $x=0\,cm$. The transient regime generated by the EHD force is responsible for eddy development from the exposed electrode. The stationary regime is reached after $600\,ms$ when the eddy has fully spread his kinetic energy due to viscosity.

Calculated velocity magnitude is around $5\,m/s$ right downstream from the end of the plasma region and decreases to less than $2\,m/s$ $5\,cm$ further away. From fig. 4.18 the y-span of the induced flow can also be evaluated. This quantity increases for higher distance from the electrode: it is about $1\,mm$ wide at the end of the plasma region and it widens to about $5\,mm$ some cms further downstream.
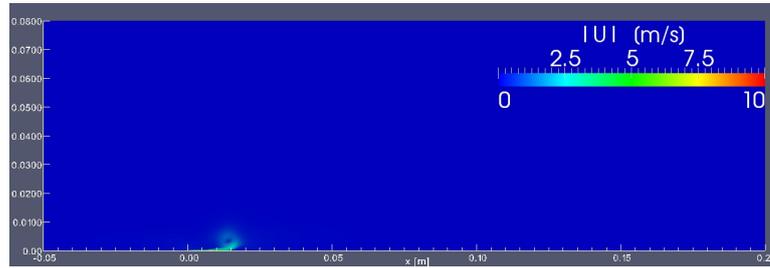
(a) *Flow velocity map (magnitude).*
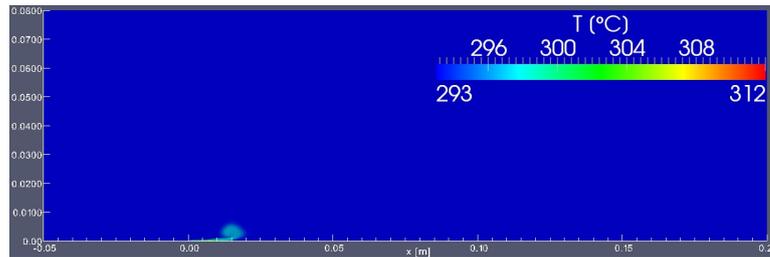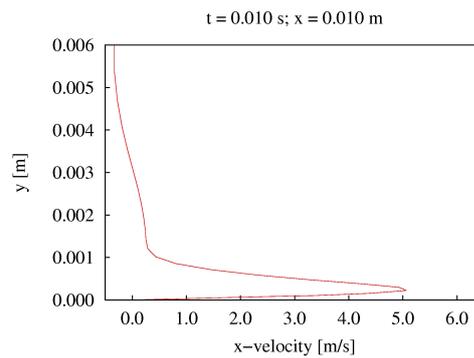
(b) *Temperature map.*
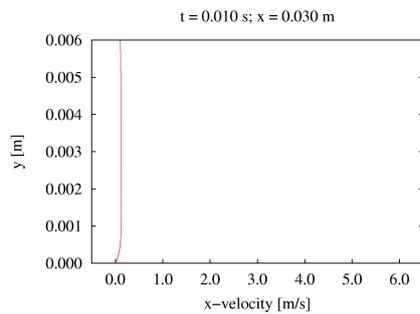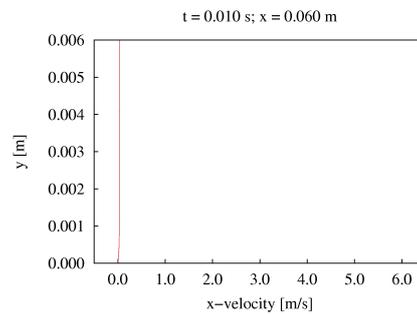
(c) $x = 0.01\,m$.

(d) $x = 0.03\,m$.


(e) $x = 0.06\,m$.

Figure 4.15: Simulated flow properties at $t = 0.010\,s$. Velocity magnitude map *(a)* and temperature map *(b)*. X-velocity line plots at different distancefrom the exposed electrode *(c,d,e)*.
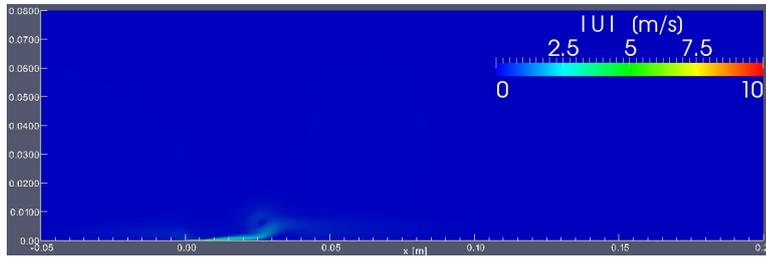
(a) *Flow velocity map (magnitude).*
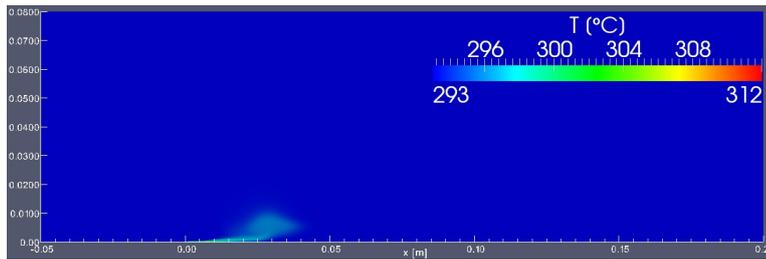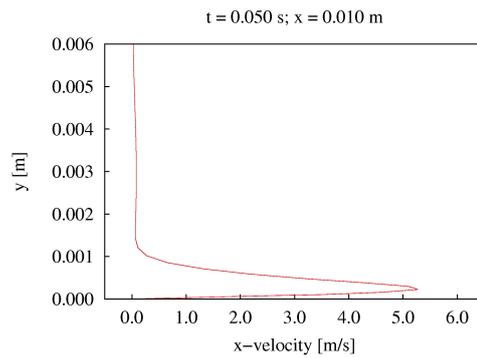
(b) *Temperature map.*
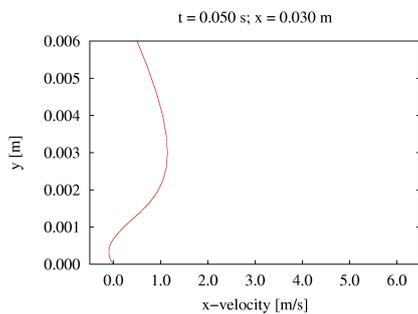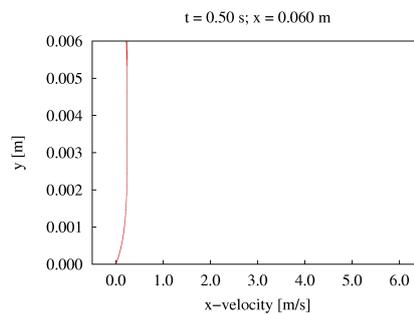
(c) $x = 0.01\,m$.

(d) $x = 0.03\,m$.

(e) $x = 0.06\,m$.

Figure 4.16: Simulated flow properties at $t = 0.050\,s$. Velocity magnitude map *(a)* and temperature map *(b)*. X-velocity line plots at different distancefrom the exposed electrode *(c,d,e)*.
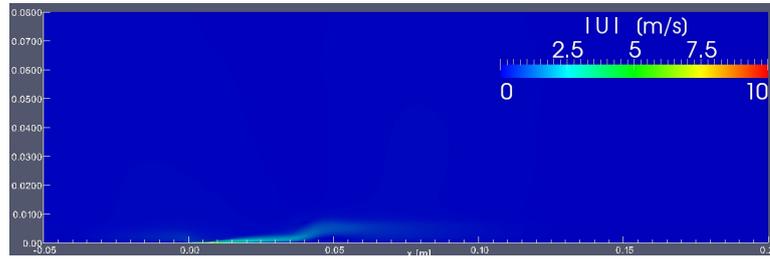
**(a)** *Flow velocity map (magnitude).*
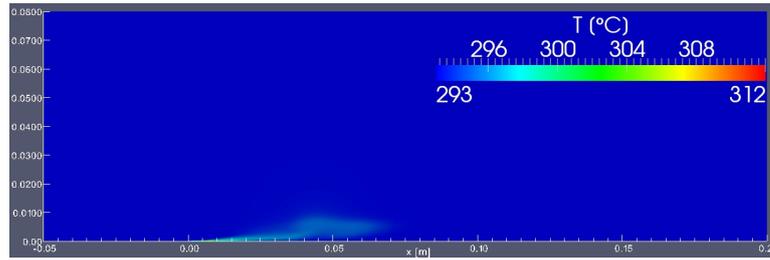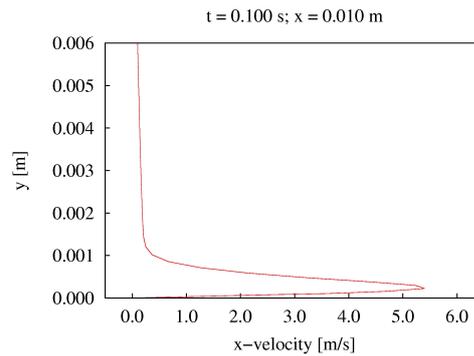
(b) *Temperature map.*
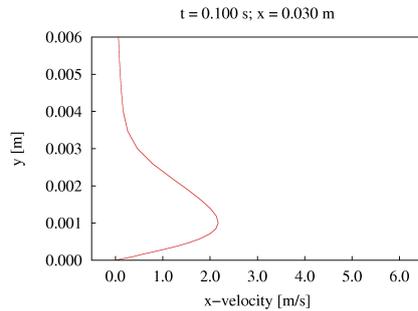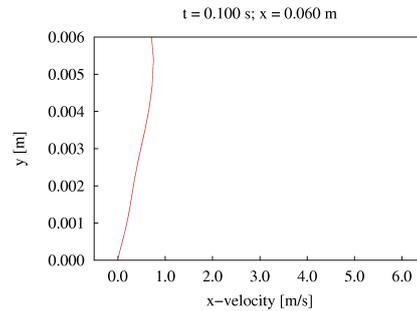
(c) $x = 0.01\,m$.

(d) $x = 0.03\,m$.

(e) $x = 0.06\,m$.

Figure 4.17: Simulated flow properties at $t = 0.100\,s$. Velocity magnitude map *(a)* and temperature map *(b)*. X-velocity line plots at different distancefrom the exposed electrode *(c,d,e)*.
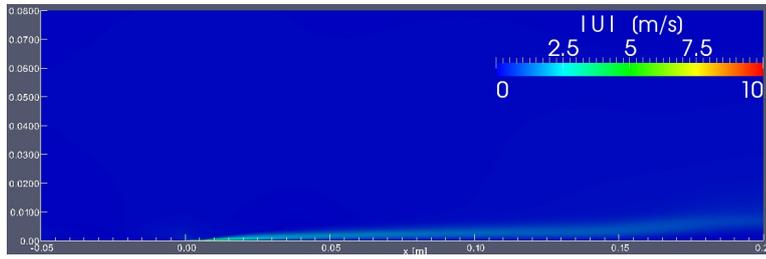
**(a)** *Flow velocity map (magnitude).*
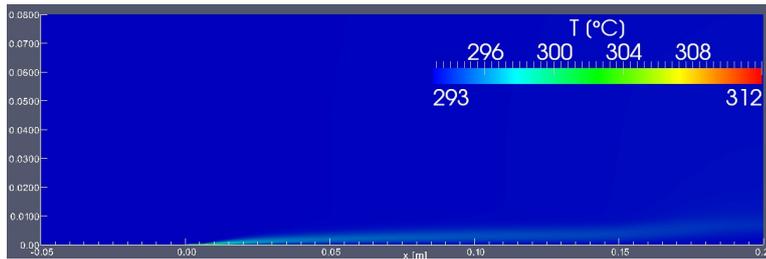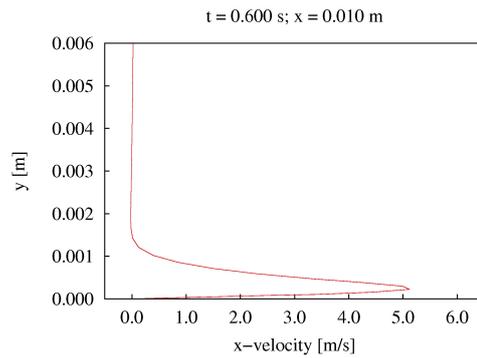
(b) *Temperature map.*

(c) $x = 0.01\,m$.
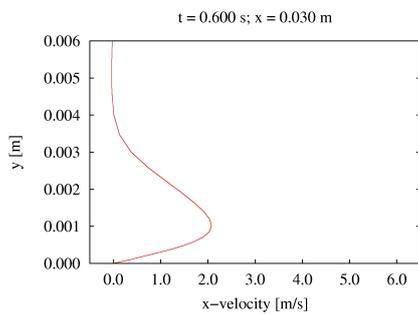
**(d)** $x = 0.03\,m$.
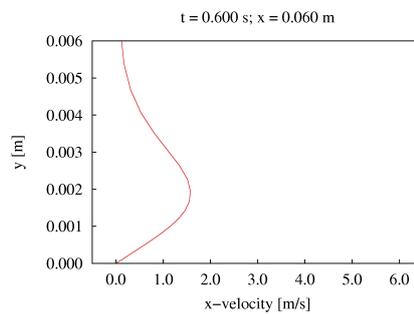
(e) $x = 0.06\,m$.

Figure 4.18: Simulated flow properties at $t = 0.600\,s$. Velocity magnitude map *(a)* and temperature map *(b)*. X-velocity line plots at different distancefrom the exposed electrode *(c,d,e)*.

Cristofolini et al. [22] measured the EHD induced flow velocity by means of the Pitot tube technique. Fig. 4.19 shows measured velocities for 3 power supply regimes which provide the same amount of power to the gas. Portraied quantities are takes at the end of the plasma region, about $1\,cm$ downstream the exposed electrode. Experimental peak values are similar to the calculated one, but measurements show that the induced flow vanishes for greater distance from the dielectric surface. Basically, good agreement between simulations and calculations arises, proving that the numerical tool described here is accurate enough to investigate basic fluid dynamic effects of DBD.
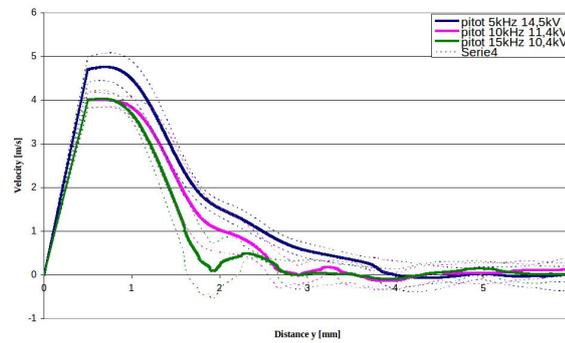

Figure 4.19: Measured velocity profiles at the end of the plasma region for different power supply regimes. x-velocity as a function of the distance from the surface is shown.

4.5   Schlieren measurements and validation

Schlieren imaging is a widely adopted plasma diagnostic technique. It provides informations about fluid density in a non-intrusive way. A so called *Z-setup* for Schlieren diagnostics is shown in fig. 4.20.

A collimated light beam is emitted and focused by parabolic off axis mirrors on the test region; following the test region, the beam is focused by a second parabolic lense on a kinfe edge and finally is collected by a PCO CCD camera equipped with a supervideo-graphics array resolution with a pixel size of $6 \times 6\ \mu m^2$. The peak quantum efficiency is 55% at a wavelength of 380 nm. The light beam path is on a plane perpendicular to the z-axis with respect to the plasma actuator displayed in fig. 2.1.
A typical Schlieren image for DBD is shown in fig. 4.21.

Cristofolini et al. [22] derived density profiles by integrating pixel intensity
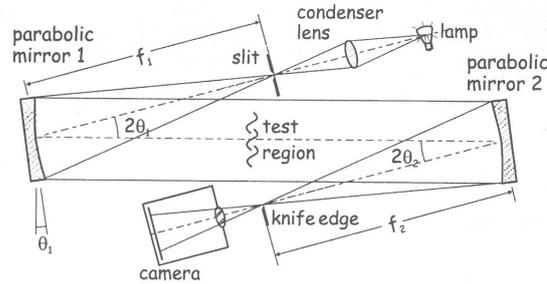
Figure 4.20: Z-configuration setup for Schlieren imaging.

Figure 4.21: Schlieren image of DBD.

of Schlieren images for DBD. The relation between Schlieren images and gas density is described as follows.

The collimated light beam is deviated because of its passing through the gas and the amount of the deviation is determined by the refractive index of the gas itself. The refractive index depends on the mass density gradients. The knife cuts from the beam all photons which are deviated more than the reference, removing them from those detected from the CCD camera. The result is a monochrome picture which makes possible to relate the pixel intensity I with the deviation and then the mass density gradients ρ:

$$I(x,y) \propto \int \frac{\partial \rho(x,y,z)}{\partial x} + \frac{\partial \rho(x,y,z)}{\partial y} dz \qquad (4.7)$$

By properly setting the diagnostic apparatus, it can be assumed that pixel intensity are due to y-gradients only. Furthermore, the plasma actuator can be considered two-dimensional, neglecting gradients in the z-direction and defining Δz the z-span of the plasma actuator which corresponds to the width of the region where the beam is deflected. This leads to the simplified relation between the pixel intensity of a Schlieren photograph of DBD and the mass density gradient:

$$I(x,y) \propto \frac{\partial \rho(x,y,z)}{\partial y} \Delta z \qquad (4.8)$$

....

By integrating eq. 4.8 along the y-direction paths as shown in fig. 4.22:

$$\int_0^y I(x, y')\, dy' \propto \Delta z \int_0^y \frac{\partial \rho(x, y')}{\partial y'}\, dy' \tag{4.9}$$

$$\int_0^y I(x, y')\, dy' \propto \Delta z\, \rho(x, y) \tag{4.10}$$
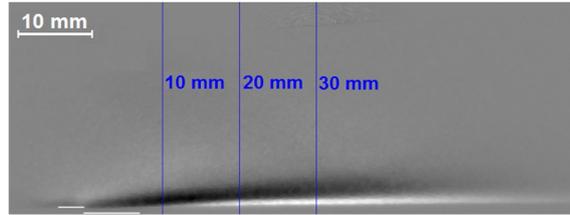

Figure 4.22: Integration paths for intensity integrals, displayed on a Schlieren image of DBD.

the proportionality relationship is expressed where the mass density is highlighted. Buondary conditions $\rho|_{x, y=\infty} = \rho_{amb}$ determine the value of the proportionality constant.

One example of pixel intensity profile taken at $3\,cm$ downstream from the exposed electrode is shown if fig. 4.23, as well as the correspondent velocity profile.

Let is define the *intensity integral $II(x, y)$* as follows:

$$II(x, y) = c_p \left[\rho_{max}(x) - \rho(x, y)\right]. \tag{4.11}$$

Intensity integrals can be evaluated from Schlieren photos according to the approach described by equation 4.9.

The most notable thing about intensity integrals obtained through Schlieren images processing is their similarity with velocity profiles measured along the integration path. It is possible to scale intensity integrals by multiplying them for a constant which is independent from the location, to reproduce velocity profiles quite accurately.

This feature is shown by fig. 4.24 where scaled intensity integrals and measured velocity profiles are compared. The equation:

$$v(x, y) = cost \times II(x, y) \tag{4.12}$$

describes the phenomena.

Two reasons lie behind this proportionality relationship: first the knife placement and second the negligibility of buoyancy effects and the predominance of forced convection in fluid motion.

. . . .
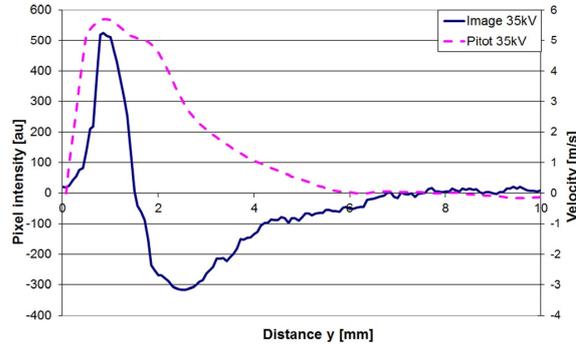
Figure 4.23: Pixel intensity (solid line) from Schlieren photographs and velocity profiles (dashed line) form Pitot measurements .
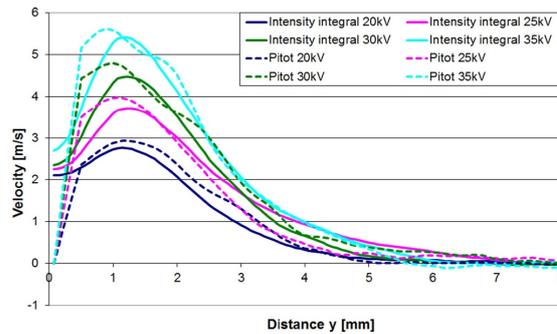

Figure 4.24: Comparison between velocity profiles (dashed line) and scaled intensity integrals (solid line) for four different power supply regimes at 30 mm form the upper electrode.

Numerical investigations were undertaken to computationally prove this effect. The OpenFOAM solver rhoPisoFoam modified as described in section 4.4 and velocity and scaled density profiles were compared at 10, 20 and 30 mm distance from the upper electrode. Fig. 4.25 shows computational results for 10 mm distance. A basically good agreement between the two curves is displayed and calculations confirm that the value of the proportionality constant is independent of the location.

This effect is rather interesting because introduces a new non intrusive diagnostic technique for studying DBD and EHD: by means of Schlieren imaging density profiles can be obtained. Properly scaling the indirectly measured density profiles gives meaningful informations about the flow velocity field. The last step to defining this promising technique is defining the proportionality constant according to the measuring setup. In order to perform this
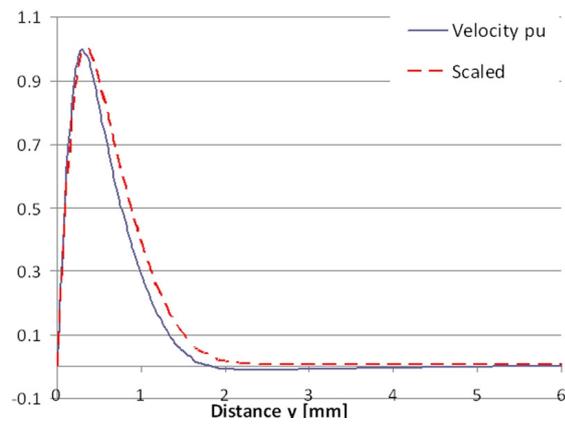
Figure 4.25: Comparison between calculated velocity profiles (solid line) and scaled intensity integrals (dashed line) at 10 mm from the upper electrode.

task numerical results need to be integrated with experimental evidences.

CHAPTER 5

CONCLUSIONS

.

Non equilibrium discharges and dielectric barrier discharge (DBD) are raising increasing engineering interest due to their flexible behavior.

The research described in this work was aimed to add some knowledge about the extremely complex environment involved with the so called EHD interaction between DBD and a superimposed gas flow. Among all DBD applications, EHD is probably one of the easiest to numerically model and simulate, because chemical composition of the discharge is believed not to be relevant. Also, a simplified model was adopted, so that single microdischarges were not simulated but the global effect of DBD was, because of the major numerical issues arising when investigating very small and short phenomena in relatively big and long space-time scales.

Nevertheless, the attempt made to duplicate EHD by coupling DBD results with a fluid dynamic code was only partially successful. Some meaningful features were effectively caught but the body force, which is the most important one, was not properly described and the calculated flow velocity did not agree with measurements.

It is believed that the failure of this approach is not due to the physical model but to the simplified assumption: not accounting for single streamers propagation leads to poor information about the discharge.

Improvements in the computational study of DBD need then to account for microdischarges evolution. Further possible improvement is the introduction of positive ions as additional charged species.

Although these difficulties demonstrate some fundamental problems, the fluid dynamic code was useful to assess the suitable features of the body force field which cause the experimentally observed flow field via an inverse process. The body force calculated in this way was in good agreement with indirectly measured force values found in literature, proving the fluid dynamic code itself is suitable for studying EHD.

The final stage of the PhD research on DBD was the validation of experimental results obtained by our research group. A new non invasive technique for studying the EHD flow field via Schlieren imaging was introduced and demonstrated.

BIBLIOGRAPHY

[1] Kip Thorne. Lecture notes from course ph 136: Applications of classical physics, 2005. Part V - Plasma Physics. vii, 7

[2] W. Siemens. Ueber die elektrostatische induction und die verzogerung des stroms in flaschendrahten. *Annalen der Physik*, 178(9):66–122, January 1857. 2

[3] U. Kogelschatz, B. Eliasson, and W. Egli. From ozone generators to flat television screens: history and future potential of dielectric-barrier discharges. *Pure and Applied Chemistry*, 71:1819–1828, 1999. 2

[4] Claire Tendero, Christelle Tixier, Pascal Tristant, Jean Desmaison, and Philippe Leprince. Atmospheric pressure plasmas: A review. *Spectrochimica Acta Part B: Atomic Spectroscopy*, 61(1):2–30, January 2006. 2

[5] B Eliasson, M Hirth, and U Kogelschatz. Ozone synthesis from oxygen in dielectric barrier discharges. *Journal of Physics D: Applied Physics*, 20:1421–1437, November 1987. 2

[6] Thomas C. Corke, Martiqua L. Post, and Dmitry M. Orlov. SDBD plasma enhanced aerodynamics: concepts, optimization and applications. *Progress in Aerospace Sciences*, 43(7-8):193–217, October. 2, 15

[7] C. A. Borghi, M. R. Carraro, A. Cristofolini, and G. Neretti. Electrohydrodynamic interaction induced by a dielectric barrier discharge. *Journal of Applied Physics*, 103:063304, 2008. 2, 26, 55

[8] Eric Moreau. Airflow control by non-thermal plasma actuators. *Journal of Physics D: Applied Physics*, 40:605–636, February 2007. 2, 26

[9] C. L. Enloe, M. G. McHarg, and T. E. McLaughlin. Time-correlated force production measurements of the dielectric barrier discharge plasma aerodynamic actuator. *Journal of Applied Physics*, 103:073302, 2008. 2, 21

[10] S M Starikovskaia. Plasma assisted ignition and combustion. *Journal of Physics D: Applied Physics*, 39:R265–R299, August 2006. 2, 16

[11] Sergey B Leonov and Dmitry A Yarantsev. Plasma-induced ignition and plasma-assisted combustion in high-speed flow. *Plasma Sources Science and Technology*, 16:132–138, February 2007. 2

[12] Danil Dobrynin, Gregory Fridman, Gary Friedman, and Alexander Fridman. Physical and biological mechanisms of direct plasma interaction with living tissue. *New Journal of Physics*, 11:115020, November 2009. 2, 15

[13] H Conrads and M Schmidt. Plasma generation and plasma sources. *Plasma Sources Science and Technology*, 9:441–454, November 2000. 8

[14] A Fridman, A Chirokov, and A Gutsol. Non-thermal atmospheric pressure discharges. *Journal of Physics D: Applied Physics*, 38:R1–R24, January 2005. 10

[15] J Hopwood. Review of inductively coupled plasmas for plasma processing. *Plasma Sources Science and Technology*, 1:109–116, May 1992. 14

[16] J. P. Boeuf and L. C. Pitchford. Electrohydrodynamic force and aerodynamic flow acceleration in surface dielectric barrier discharge. *Journal of Applied Physics*, 97:103307, 2005. 15, 32, 33

[17] A R Hoskinson, N Hershkowitz, and D E Ashpis. Force measurements of single and double barrier DBD plasma actuators in quiescent air. *Journal of Physics D: Applied Physics*, 41:245209, December 2008. 15

[18] M Klein, N Miller, and M Walhout. Time-resolved imaging of spatiotemporal patterns in a one-dimensional dielectric-barrier discharge system. *Physical Review. E, Statistical, Nonlinear, and Soft Matter Physics*, 64(2 Pt 2):026402, August 2001. PMID: 11497706. 21

[19] A R Hoskinson and N Hershkowitz. Differences between dielectric barrier discharge plasma actuators with cylindrical and rectangular exposed electrodes. *Journal of Physics D: Applied Physics*, 43:065205, February 2010. 21

[20] C. Enloe, T. McLaughlin, R. Van Dyken, K. Kachner, E. Jumper, and T.C. Corke. Mechanisms and responses of a single dielectric barrier

plasma actuator: Plasma morphology. *AIAA Journal 2004*, 42(3):589–594. 21, 25, 26

[21] C. Enloe, T. McLaughlin, R. Van Dyken, K. Kachner, E. Jumper, T.C. Corke, and O. Haddad. Mechanisms and responses of a dielectric barrier plasma actuator: Geometric effects. *AIAA Journal 2004*, 42(3):595–604. 21, 26

[22] A. Cristofolini, G. Neretti, F. Roveda, and C. A. Borghi. Schlieren imaging in a dielectric barrier discharge actuator for airflow control. *Journal of Applied Physics*, 111(3):033302, 2012. 23, 28, 55, 60

[23] Dmitry F. Opaits, Alexandre V. Likhanskii, Gabriele Neretti, Sohail Zaidi, Mikhail N. Shneider, Richard B. Miles, and Sergey O. Macheret. Experimental investigation of dielectric barrier discharge plasma actuators driven by repetitive high-voltage nanosecond pulses with dc or low frequency sinusoidal bias. *Journal of Applied Physics*, 104:043304, 2008. 25, 26

[24] Flint O. Thomas, Thomas C. Corke, Muhammad Iqbal, Alexey Kozlov, and David Schatzman. Optimization of dielectric barrier discharge plasma actuators for active aerodynamic flow control. *AIAA Journal*, 47:2169–2178, Sep 2009. 26

[25] V. R. Solovâev, A. M. Konchakov, V. M. Krivtsov, and N. L. Aleksandrov. Numerical simulation of a surface barrier discharge in air. *Plasma Physics Reports*, 34:594–608, July 2008. 31

[26] J. S. Shang, P. G. Huang, H. Yan, and S. T. Surzhikov. Computational electrodynamic simulation of direct current discharge. *Journal of Applied Physics*, 105(2):023303, 2009. 34, 35, 44

[27] J. S. Shang and P. G. Huang. Modeling of ac dielectric barrier discharge. *Journal of Applied Physics*, 107(11):113302, 2010. 35, 44

[28] J. S. Shang, F. Roveda, and P. G. Huang. Electrodynamic force of dielectric barrier discharge. *Journal of Applied Physics*, 109:113301, 2011. 35

[29] A. R. Hoskinson, L. Oksuz, and N. Hershkowitz. Microdischarge propagation and expansion in a surface dielectric barrier discharge. *Applied Physics Letters*, 93:221501, 2008. 44